INL/EXT-17-41677
Revision 0

Testing Fast Reactor Fuels in a Thermal Reactor:
A Comparison Report

Nuclear Technology Research and Development

Jason M. Harp
Steven L. Hayes
Pavel G. Medvedev
Douglas L. Porter
Luca Capriotti

Prepared for
U.S. Department of Energy
Advanced Fuels Campaign

Idaho National Laboratory
September 2017
NTRD-FUEL-2017-000148

DISCLAIMER

SUMMARY

The testing of fast reactor fuels in the thermal-spectrum of the Advanced Test Reactor using cadmium-filtering has been underway since 2003. The objective of this experimental approach to create a temperature profile inside of test fuel rodlets that is nearly prototypic of corresponding fast reactor conditions. This requires, necessarily, that the power generation profile inside of test fuel rodlets also be nearly prototypic of corresponding fast reactor conditions. By doing so, this experimental approach should allow for the study of fast reactor fuel performance phenomena that are primarily dependent upon the conditions of temperature and/or temperature gradient inside the fuel to be possible using a thermal test reactor. Validation of this assertion has been undertaken by both supporting analyses and by comparing fuel performance phenomena observed in fuels irradiated in cadmium-filtered positions in ATR to similar or identical fuels irradiated under similar conditions in genuine fast reactors.

This report documents a preliminary comparison of fuel performance data available from the testing of metallic, oxide, and nitride fuels in cadmium-filtered positions in the ATR to the performance of identical or similar fuels irradiated in genuine fast reactors. Although a variety of fuel performance metrics are presented, particular attention is paid to those phenomena that are primarily, or significantly, dependent on conditions of temperature and temperature gradient with the fuel. Although the comparisons presented in this report are at this time limited in scope and preliminary in nature, they do support the assertion that the objectives of the cadmium-filtered testing approach in ATR are both feasible and appear sound. The analyses and comparisons presented in this report show that ATR irradiations performed using cadmium shrouding are sufficiently prototypic that they can be used with confidence in the development and testing of fast reactor fuels.

INTENTIONALLY BLANK

CONTENTS

FIGURES

TABLES

INTENTIONALLY BLANK

ACRONYMS

AFC	Advanced Fuels Campaign
AL	Analytical Laboratory
ATR	Advanced Test Reactor
bcc	Body Centered Cubic
BSE	Back-scattered Electron
DOE	Department of Energy
EBR-II	Experimental Breeder Reactor II
EDM	Electrical Discharge Machine
EML	Electron Microscopy Laboratory
EPMA	Electron Probe Micro-Analysis
FCCI	Fuel-cladding Chemical Interaction
FFTF	Fast Flux Test Facility
FIB	Focused Ion Beam
FIMA	Fissions per Initial heavy Metal Atoms
FTA	Actinide Transmutation Fuels
GASR	Gas Assay, Sample, and Recharge
GECT	Gamma Emission Computed Tomography
HFEF	Hot Fuel Examination Facility
ICP-MS	Inductively Coupled Plasma, Mass Sepctrometry
IFR	Integral Fast Reactor
INL	Idaho National Laboratory
LHGR	Linear Heat Generation Rate
NRAD	Neutron Radiography Reactor
PIE	Postirradiation Examination
PGS	Precision Gamma Scanner
SEM	Scanning Electron Microscope
SFR	Sodium Fast Reactor
TEM	Transmission Electron Microscope
XRD	X-Ray Diffraction

INTENTIONALLY BLANK

TESTING FAST REACTOR FUELS IN A THERMAL REACTOR: A COMPARISON REPORT

1. INTRODUCTION

Since 2003 Idaho National Laboratory has been performing irradiation testing of a variety of metallic, oxide, and nitride fuels as part of a research program investigating fuels for advanced nuclear reactors, including fuels with the potential for actinide transmutation [1]. This activity supports the objective to develop sustainable nuclear fuel cycles as outlined in the DOE Nuclear Energy Research and Development Roadmap [2]. It is expected that current research and development efforts will culminate in a suite of options that will enable future decision makers to make informed choices about how best to manage used fuel from nuclear reactors. In this context, irradiation testing of advanced fast reactor and transmutation fuels supports development of the full recycle technology option that would allow repeated recycling of transuranic elements in fast-spectrum reactors for their eventual destruction, substantially reducing the need for the geologic disposal of transuranic waste.

Advanced reactor fuel development activities in the Advanced Fuels Campaign (AFC) have included the design, fabrication, irradiation, and postirradiation examination of metallic, oxide, and nitride fuels. While access to a fast-spectrum test reactor is essential in order to advance this research activity to a fuel technology qualified for reactor use, recent technology readiness guidelines [3] indicate that proof-of-concept irradiation testing can be performed using test reactors where irradiation conditions are not fully prototypic of the intended reactor application. As the scope of proof-of-concept irradiation testing is limited to fuel candidate selection [4], budget, schedule, and practicality considerations led to utilization of the Advanced Test Reactor (ATR) for the proof-of-concept irradiation testing of transmutation fuels. Despite being a thermal-spectrum test reactor, ATR is attractive for transmutation fuel testing due to its relatively high fast flux, the historic ability to tailor the fast-to-thermal flux ratios using thermal neutron filtering concepts, and the ability to operate at varying power levels in different regions of the core. Neutron flux tailoring has been used extensively in the ATR using fixed and removable shrouds [5]. For the purposes of irradiation testing of advanced reactor and transmutation fuels, removable cadmium shrouds 0.114 cm (0.045-in.) in thickness are used to filter out >97% of the thermal flux seen by the test articles. The methods and results of the underlying neutron physics analysis describing how the ATR neutron flux is tailored for irradiation testing of the transmutation fuels has been described elsewhere [6, 7]. Other historical precedent for the use of cadmium to filter thermal neutron flux for the purposes of fast reactor fuel testing dates back to the 1960s, when cadmium screens were used in BR2 testing of liquid metal fast breeder reactor fuel pins under transient operating conditions [8].

From the perspective of testing fuel performance, the principal difference between irradiation of transmutation fuels in a fast versus thermal neutron spectra is in how the resulting fission power density is distributed radially within a metallic fuel slug or ceramic fuel pellet. Under the fully prototypic irradiation conditions achieved in a fast reactor, the power density distribution in the fuel is essentially uniform and independent of fuel radius since the mean free path of fast neutrons is much larger than the dimensions of a fuel pin. In the neutron spectrum of a thermal reactor such as ATR, the radial power density distribution within a fuel pin exhibits significant peaking at the fuel periphery, with a corresponding depression at the fuel center, due to self-shielding, which is attributed to the presence of resonance cross sections of uranium and plutonium isotopes at low neutron energies. Use of cadmium shrouds results in the capture of a vast majority of thermal neutrons by cadmium, greatly reducing self-shielding in the test fuels. Detailed comparison analyses between the cadmium shroud-hardened neutron spectrum in the ATR and in a typical fast reactor has been reported by Chang in reference 6. It was found that transmutation fuels irradiated in a fast reactor would exhibit a radial peaking factor of 1.01, as compared to 2.34 in an unshrouded configuration in the ATR and 1.23 in a Cd-shrouded configuration in the ATR. While characterization of the radial peaking factors for the neutron spectra of interest illustrates the efficiency of the cadmium shrouds, the relevancy of the irradiation experiments must be further demonstrated by evaluating fuel temperatures achieved during ATR cadmium-shrouded irradiations of transmutation fuels to those that would be expected in a fast reactor and by comparing fuel behaviors in identical or similar fuels irradiated in both configurations [7].

This report documents the use of radial power density distributions to evaluate corresponding radial temperature distributions in the Cd-shrouded irradiation vehicles used for irradiation testing of advanced reactor and transmutation fuels in ATR and to perform comparisons of the behavior of both metallic and oxide fuels to similar irradiations conducted a fast reactor. This activity has been undertaken in an effort to establish the relevancy of fuel performance data generated for fast reactor fuels using ATR cadmium-shrouded experiments.

2. ANALYSIS OF SHROUDED IRRADIATION CONDITIONS

2.1 Cadmium Shroud Description/Approach

The goal of this section is to utilize the radial power density distributions previously reported by Chang [7] to evaluate corresponding radial temperature distributions in the cadmium-shrouded irradiation vehicles used for irradiation testing of transmutation fuels and perform comparison to irradiations in a fast reactor. Formation of the columnar grain region in fast reactor oxide fuels can be easily measured during post irradiation examination (PIE), allowing determination of the fuel temperature on the outer boundary of the columnar grain region. Therefore, modeling of the columnar grain region formation and comparison of model results to the PIE is an established practice to validate thermal analysis of fast reactor oxide fuel. This is important for establishing the relevancy of the experimental data generated by the DOE's Advanced Fuels Campaign. Ideally, validation would be shown on oxide, metallic, and nitride fuels. At this time, the available BISON models for oxide fuels are more developed and ready for use in validation exercises. As models for metallic and nitride fuel are further developed, additional validation exercises may be added to future versions of this report. A cross section showing the dimensions of the Cd-shrouded irradiation position used in AFC-1 and AFC-2 is shown in Figure 1. The neutron energy spectrum created in a Cd shrouded positions as predicted by Chang is shown in Figure 2, and this figure also contains a spectrum from a Sodium Fast Reactor.

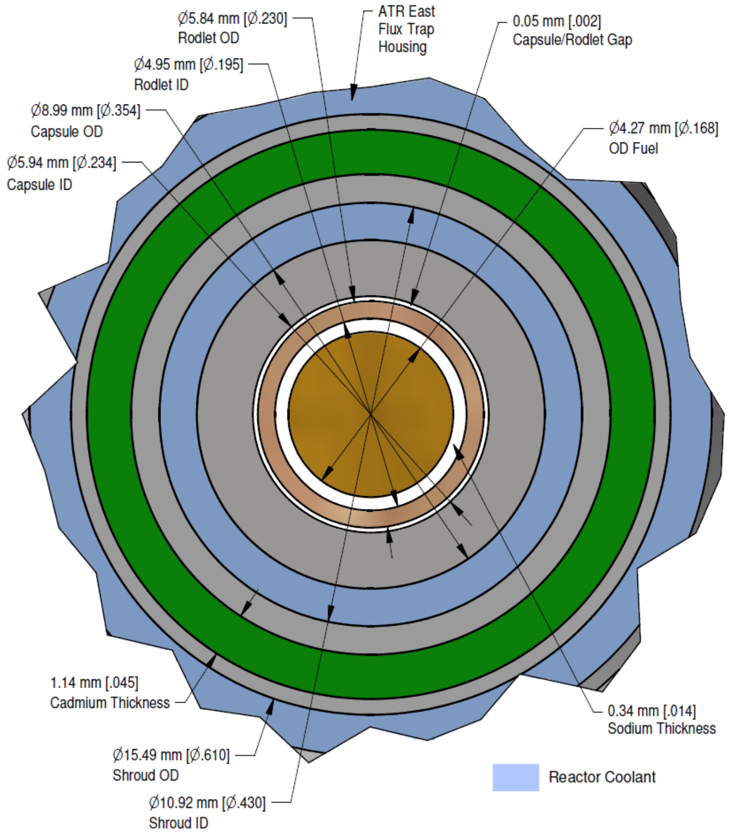

Figure 1. Cross section of the Cd shrouded experiments used in AFC-1 and AFC-2

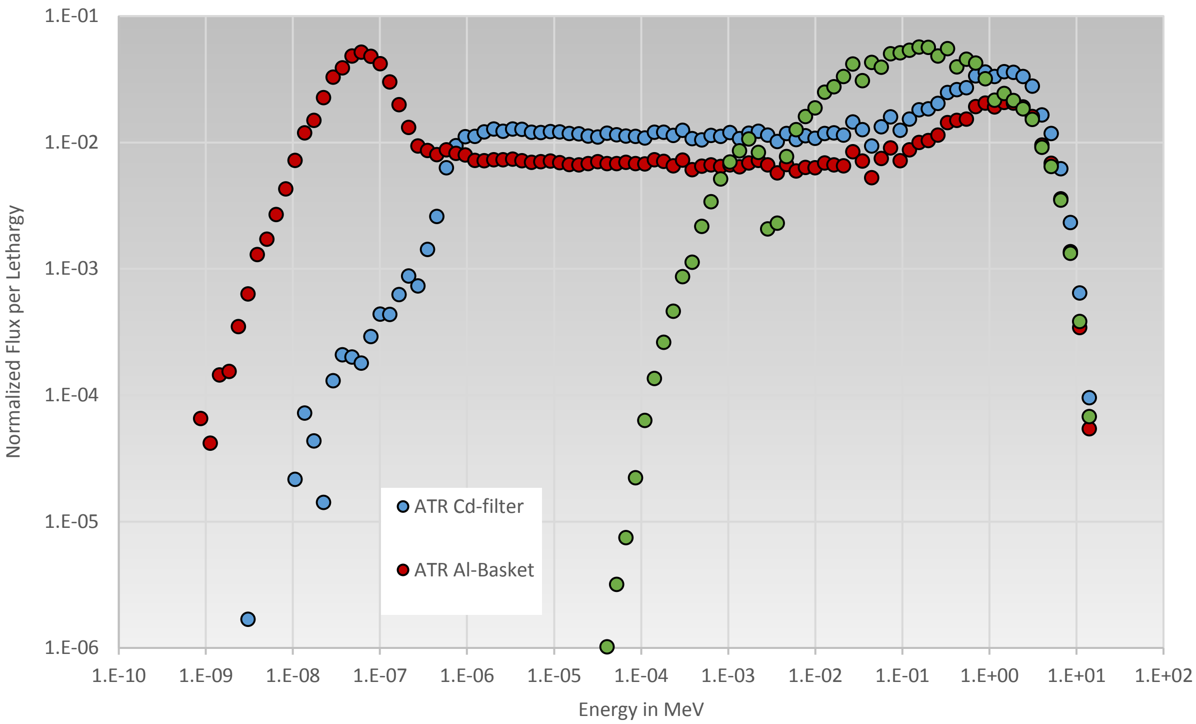

Figure 2. Neutron Spectrum in an ATR Position, a Cd Shrouded Position, and a prototypic Sodium Fast Reactor (SFR)

2.2 Radial Flux Profile, Temperature Profile - Comparison of the Radial Power Profiles in Representative Transmutation Fuels Irradiated in Thermal, Fast and Cadmium-Filtered Neutron Flux

Comparison of the beginning-of-life simulated radial power profiles in the metallic transmutation fuel irradiated in thermal, fast and cadmium-filtered neutron flux previously reported by Chang [6, 7] is shown in Figure 3. These results are for the metallic fuel with the composition U-29Pu-4Am-2Np-30Zr irradiated as a part of the AFC-1F test. Simulated radial power profiles for the oxide fuel (AFC-2C having the composition U-17Pu-2.4Am-1.3Np-12.3O are shown in Figure 4. As evident from Figure 3 and Figure 4, radial peaking is slightly less pronounced in the oxide, primarily because of the lower density of oxide compared to metallic fuels. The effect of the depletion of the Cd throughout two typical ATR cycles is shown in Figure 5.

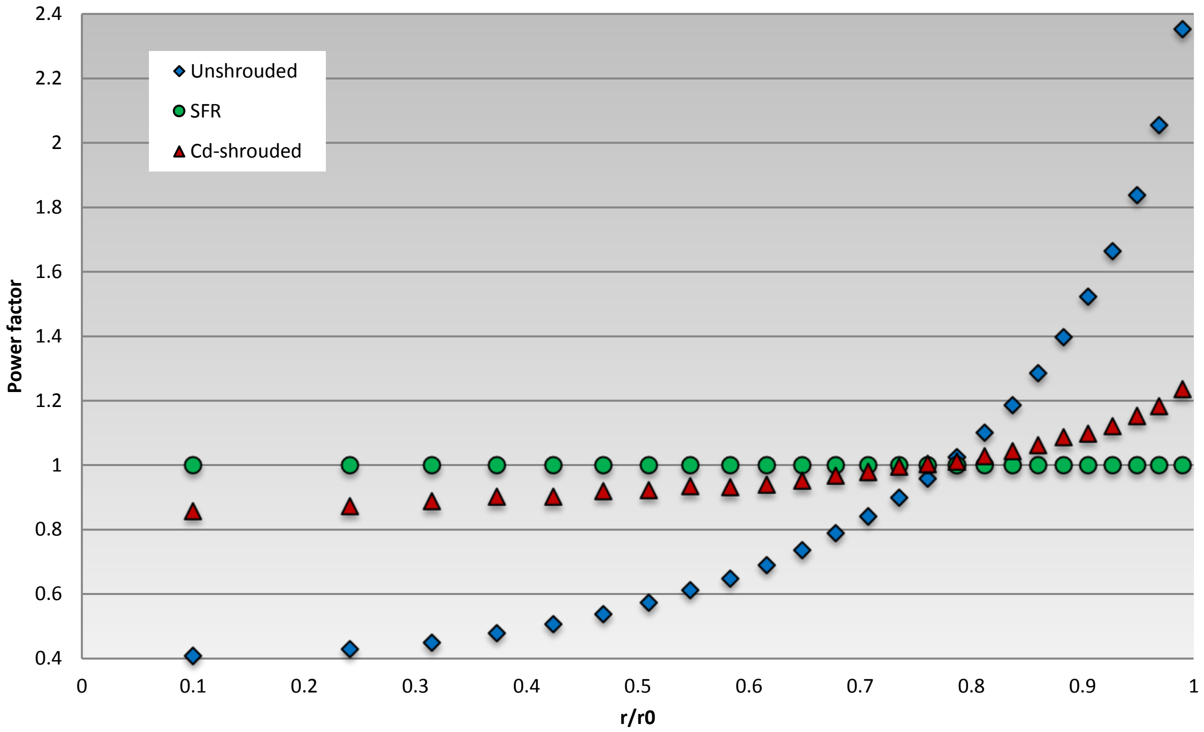

Figure 3 Comparison of the radial power profiles in metallic fuel irradiated in thermal, fast and Cd filtered thermal neutron spectra

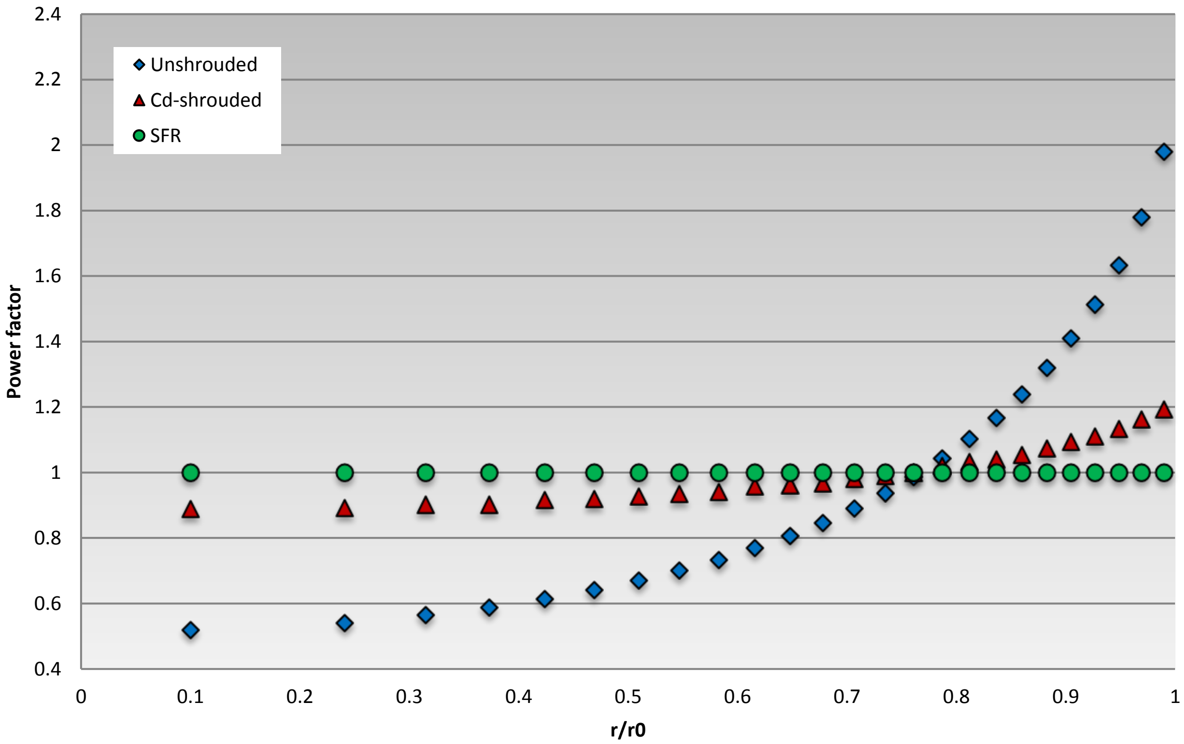

Figure 4. Comparison of the radial power profiles in oxide fuel irradiated in thermal, fast and Cd-filtered thermal neutron spectra.

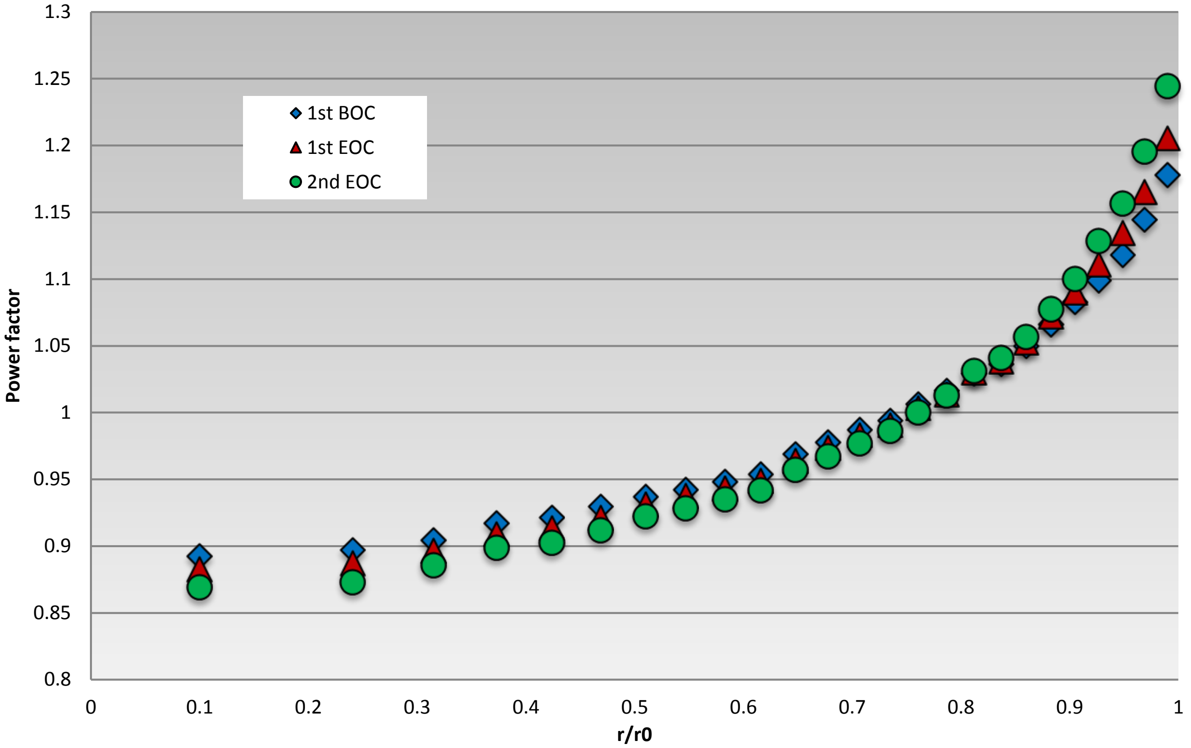

Figure 5. Comparison of the radial power profiles in oxide fuel as it is irradiated in Cd-filtered thermal neutron spectra over 2 ATR cycles.

2.3 Experiment Power History and Temperature - Comparison of the Fuel Temperatures of the Representative Transmutation Fuels Irradiated in Thermal, Fast and Cadmium-filtered Neutron Flux

2.3.1 Comparison of Measured Columnar Grain Region Diameter Observed During PIE of AFC-2C (MOX Fuel) Experiment with Calculation

In oxide fuels, columnar grains are formed because of the migration of the pores up the temperature gradient by evaporation-condensation mechanism [9]. Evaporation-condensation mechanism is thermally activated; therefore, presence of the columnar grains in the PIE images is an indicator that local fuel temperature has exceeded the threshold necessary for the pore migration to commence. Comparison of the measured columnar grain region diameter observed during post irradiation of fast reactor oxide fuels with a calculation has been historically used to validate thermal analysis of fast reactor oxide fuel [10]. The predicted radial temperature profile of AFC-2C MOX Fuel in a Cd-shrouded position neutron spectrum compared to a SFR and an unshrouded position neutron spectrum is shown in Figure 6. This show that the correct temperature profile is established to result in significant fuel restructuring. In this study, columnar grain region diameter was calculated using the BISON fuel performance code. Results of the calculation are compared with the measurement in Table 1. As evident from Table 1, BISON slightly under predicted columnar grain region diameter. Given the uncertainties associated with the design parameters, behavior models, and material properties, neutron physics results input into the BISON model, it is concluded that this comparison adequately validates the BISON thermal analysis of the AFC-2C experiment. Since radial power distribution discussed in Section 0.2 was used to model volumetric heat generation in the fuel, the present calculation demonstrates validity of the radial power distribution as well.

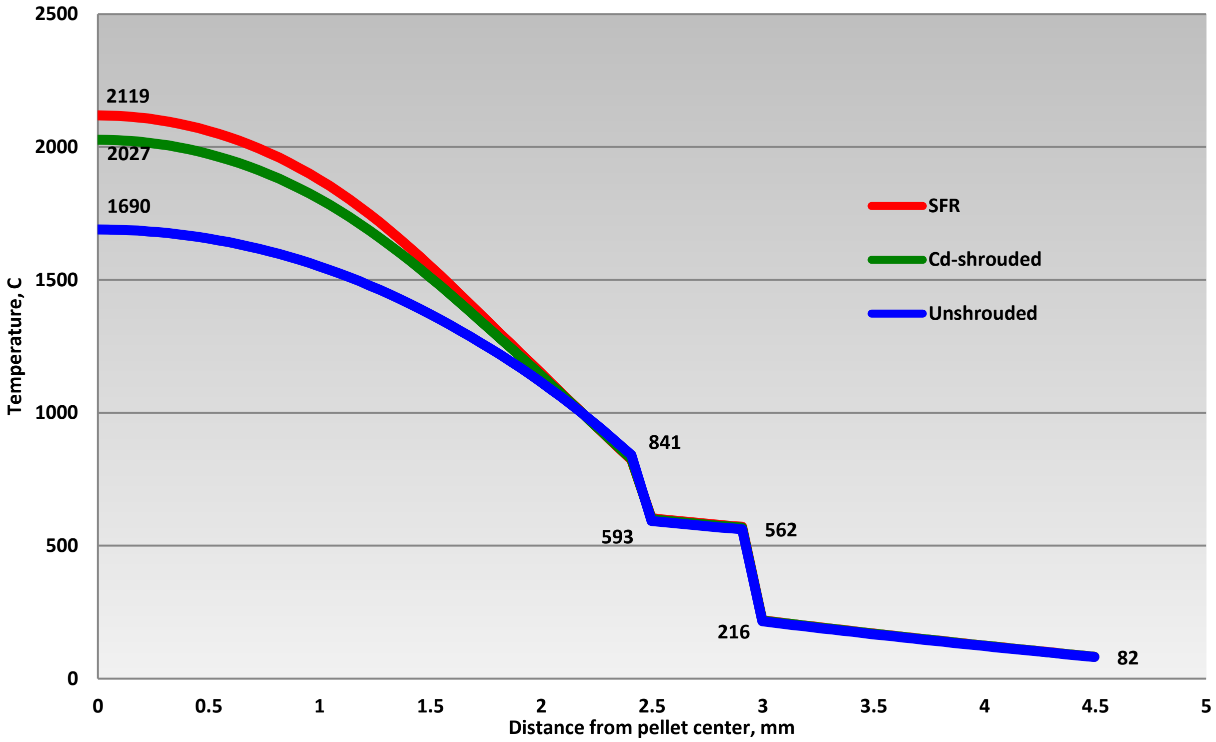

Figure 6. Radial temperature profile in AFC-2C generated by different neutron energy spectra.

Table 1. Comparison of the measured columnar grain region diameter observed during post irradiation examination of AFC-2C experiment with calculation.

Rodlet ID	Measured Columnar Grain Region Diameter mm	Calculated Columnar Grain Region Diameter mm
AFC-2C-R2	2.73	2.52
AFC-2C-R3	3.7	3
AFC-2C-R4	3.08	2.72
AFC-2C-R6	0	0

2.3.1.1 Impact of Neutron Flux Energy Spectrum on the Diameter of the Columnar Grain Region in AFC-2C Experiment

To illustrate the impact of neutron flux energy spectrum on the diameter of the columnar grain region, BISON was utilized to calculate diameter of the columnar grain region in the following hypothetical configurations: (1) AFC-2C experiment irradiated in an unfiltered ATR neutron flux, and (2) sodium fast reactor (SFR) neutron flux. Results of these calculations are shown in Table 2 for comparison against the measured value of columnar grain region diameter. They clearly demonstrate the significance of the cadmium filter for achieving irradiation conditions in ATR prototypic of an SFR. Irradiation in unfiltered ATR neutron flux does not produce a columnar grain region in the AFC-2C experiment while irradiation in Cd-filtered ATR spectrum produces columnar grain region whose diameter is 7% smaller than SFR.

Table 2. Impact of neutron flux energy spectrum on the diameter of the columnar grain region.

Parameter	Unfiltered ATR neutron flux	ATR Cd-filtered neutron flux	SFR
Columnar grain region diameter, mm	0	2.73	2.72

Impact of neutron flux energy spectrum on the diameter of the columnar grain region is further demonstrated by plotting the columnar grain region diameter as a function of the linear heat generation rate (LHGR) as shown in Figure 7. According to Figure 7, in Cd-filtered and in SFR neutron spectra the columnar grain region begins to form when LHGR reaches approximately 250 W/cm. It takes LHGR of 315 W/cm to initiate restructuring if irradiation were to be conducted in unfiltered ATR spectrum. The fact that fuel restructuring behavior in a cadmium-filtered spectrum nearly tracks that in an SFR is compelling evidence that irradiation of fuels in the cadmium-filtered ATR spectrum produces a radial temperature profile that must be very similar to what is experienced in a fast neutron spectrum of a genuine SFR.

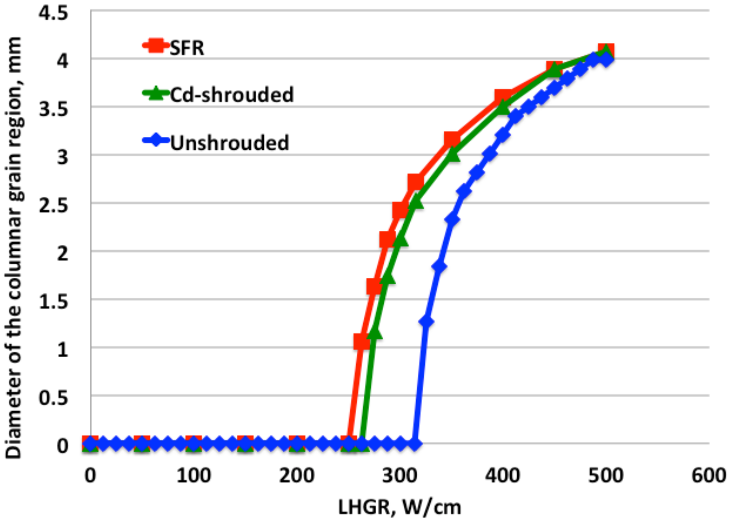

Figure 7. Columnar grain region diameter, as calculated by BISON, as a function of the linear heat generation rate (LHGR).

2.3.1.2 Comparison of the AFC-2C Experiment Thermal Performance with a Fast Flux Test Facility (FFTF) Full Size Fuel Pin

Comparison of the calculated AFC-2C experiment thermal performance irradiated in cadmium filtered ATR spectrum with the thermal performance of an FFTF full size fuel pin is shown in Figure 8 and Figure 9. Excellent agreement between the peak fuel temperatures at LHGR above 300 W/cm is evident form Figure 8. As shown in Figure 9, cladding temperatures exhibit some agreement in the LHGR interval between 300 and 400 W/cm. The AFC-2 experiment seems to run significantly colder than FFTF fuel rod at low LHGR due to lower ATR coolant temperature and a low temperature increase over the cladding-capsule gas gap for lower LHGR. It is also noted that at the peak cladding temperature in the AFC-2C experiment is significantly higher when LHGR approaches 500 W/cm due to increasing thermal resistance of the cladding capsule gas gap with LHGR. Despite striking differences between FFTF and ATR use of cadmium filtering and double encapsulation allows sufficiently prototypic irradiation conditions to be achieved in ATR for successful proof-of-concept testing of fast reactor fuels.

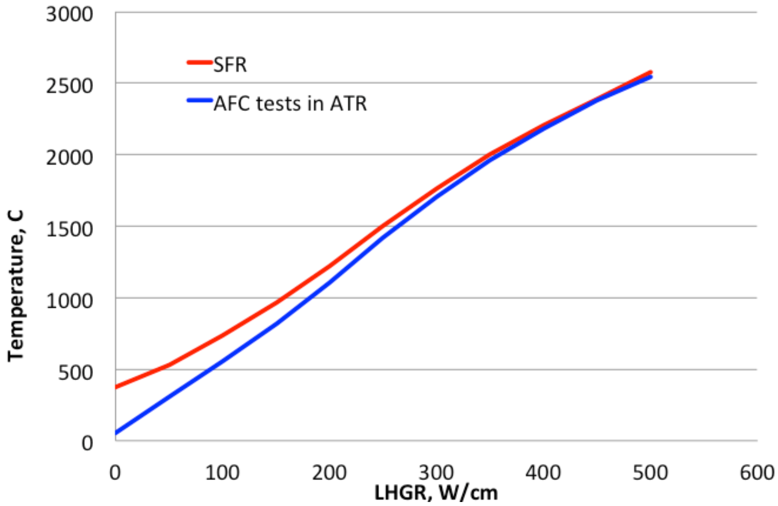

Figure 8. Comparison of calculated peak fuel temperature in AFC-2C experiment and in an FFTF full size fuel pin.

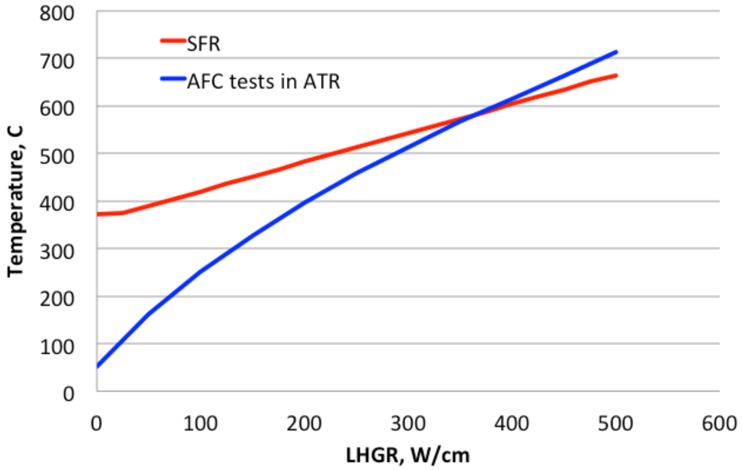

Figure 9. Comparison of calculated peak cladding temperature in AFC-2C experiment and in an FFTF full size fuel pin.

2.4 Summary of Cd Shrouded Irradiation Testing Analysis

The present study presents evidence that use of cadmium filtering allows irradiation conditions in the ATR suitable for fast reactor fuel testing. The study showed how formation of the columnar grain region in oxide fuels is impacted by the radial power distribution in the fuel. In an unfiltered ATR neutron spectrum the power shifts to the pellet periphery requiring higher LHGR to achieve formation of the columnar grain region. Use of cadmium filtering results in capture of the thermal neutrons which flattens out the radial power distribution in the fuel, similar to the flat radial power distribution known to exist in an SFR. This effect was demonstrated by modeling formation of the columnar grain region in filtered ATR and SFR neutron spectra and confirmation of the similarity of fuel behavior in these two configurations.

Recognizing that modeling of the columnar grain region formation is an established practice to validate thermal analysis of fast reactor oxide fuel, the results of this study provide foundation for establishing relevancy of the proof-of-concept testing of transmutation fuels in the ATR.

3. PIE COMPARISONS

Postirradiation Examination (PIE) results from the examination of the FUTURIX-FTA irradiation experiment conducted in the Phénix fast reactor and sister pins from the AFC-1 experiments conducted in the ATR are presented in this chapter. Although a discussion of the particular characteristics of the Phénix fast reactor and ATR are beyond the scope of this report, such descriptions can be found elsewhere [11, 12]. Additionally, other irradiation experiments from the AFC series of irradiation tests are compared to literature and historic results from other fast reactors, particularly EBR-II and FFTF. Irradiation of MOX fuel in the AFC series is compared with literature. As additional data becomes available, additional comparisons will be added to future revisions of this report.

3.1 FUTURIX-FTA (DOE1,2,3,4) vs AFC-1

The FUTURIX-FTA irradiation experiment was designed to study the fuel performance of candidate transmutation fuels. The purpose of proposed transmutation fuel forms is reduction of the radio-toxicity of future high level waste destined for disposal in geologic repositories. The objective, then, of transmutation fuel development is a demonstrated fuel concept and qualified fuel design that accomplishes transmutation while meeting system requirements. Toward that end, the FUTURIX-FTA irradiation experiment was designed to study the fuel performance of candidate transmutation fuels. The FUTURIX-FTA experiment was conducted in the genuine fast neutron spectrum conditions of the Phénix sodium fast test reactor in France. FUTURIX-FTA contained several fuel compositions that were also irradiated as part of the AFC-1 test series in cadmium-filtered positions in the Advanced Test Reactor (ATR) at Idaho National Laboratory (INL) in an attempt to approximate thermal conditions experienced by a fuel pin in a fast reactor [13, 14]. The compositions of the FUTURIX-FTA pins and the AFC-1 rodlets were designed to investigate if minor actinides could be incorporated into the fuel of a fast reactor without significantly degrading fuel performance, as understood for previously well studied fuels. The general performance of metallic fuel in fast reactors has been well documented [15, 16, 17, 18, 19]. Likewise the irradiation performance of nitride fuels in fast reactors has also been documented, although the existing database for nitride fuels is much smaller than the database for metal fuels [20].

PIE from the FUTURIX-FTA irradiations [21] provides important data to assess whether the testing of fast reactor fuels using an ATR cadmium-filtered spectrum adequately reproduces fuel behaviors known to result in a true fast spectrum reactor like Phénix, or if there are tangible differences that need to be considered when evaluating fuel performance based on ATR cadmium-filtered testing. FUTURIX-FTA pins consisted of a 35.2 cm miniature fuel rod (rodlet) with extensions welded to the top and bottom of each rodlet in order to position the test rodlet at the desired axial location in the core. A sketch of the fuel rodlet is shown in Figure 10. The fuel pin cladding is AIM1 [22, 23], an austenitic stainless steel provided by CEA as the standard Phénix cladding. The rodlets used in the AFC-1 cadmium-filtered tests were 15.24 cm in length, and typical configurations are shown in Figure 11. The cladding for these rodlets was HT-9 ferritic-martensitic steel. Compositions of FUTURIX-FTA and corresponding sister AFC-1 rodlets are listed in the Table 3, and the calculated irradiation conditions experienced by these rodlets in reactor are given in Table 4. Detailed PIE of FUTURIX-FTA occurred at the INL Hot Fuel Examination Facility (HFEF) and other associated facilities. The baseline PIE of FUTURIX-FTA is documented in Reference 21. The baseline PIE conducted on the AFC-1 rodlets is documented in Reference 13 for low burnup rodlets and 14 for higher burnup rodlets.

In the following sections PIE results from FUTURIX-FTA pins and AFC-1 rodlets having similar compositions and fission densities will be compared. Relevant examinations included visual inspection of the test pins, neutron radiography, cladding profilometry, gamma ray spectrometry, fission gas release and analysis, optical microscopy, and burnup analysis by analytical chemistry. More detailed examinations on samples from these test fuels planned for the future will also be documented. This includes future work with electron microscopy utilizing scanning electron microscopes (SEM), electron micro-probe analyzers (EPMA), and transmission electron microscopes (TEM).

Table 3. Composition of FUTURIX Rodlets and Sister AFC-1 Rodlets

Name	Fuel Type	Composition* [24, 25]	AFC Rodlets
DOE1	Metallic low fertile	U-28.3Pu-3.8Am-2.1Np-31.7Zr [U-29Pu-4Am-2Np-30Zr]	AFC-1F: 1, 4 AFC-1H: 1, 4
DOE2	Metallic non-fertile	Pu-10.5Am-0.3Np-41.6Zr [Pu-12Am-40Zr]	AFC-1B: 1, 4 AFC-1D: 1, 4 AFC-1G: 1, 4
DOE3	Nitride low fertile	$(U_{0.51}Pu_{0.27}Am_{0.14}Np_{0.08})N$ $[(U_{0.50}Pu_{0.25}Am_{0.15}Np_{0.10})N]$	AFC-1Æ: 6 AFC-1G: 3
DOE4	Nitride non-fertile	$(Pu_{0.85}Am_{0.15})N$+46.5ZrN $[(Pu_{0.50}Am_{0.50})N$+36ZrN]	AFC-1Æ: 1, 3, 4

*numbers preceding elements denote weight percent, subscript numbers represent mole percent. This is the as-fabricated composition followed by the nominal composition in brackets

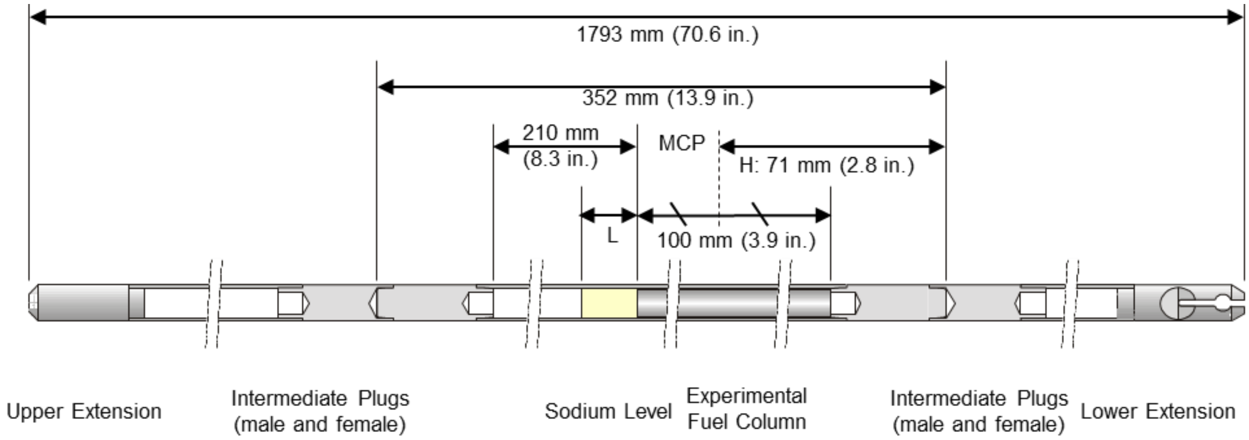

Figure 10. FUTURIX-FTA rodlet configuration and design dimensions. The outer diameter of the cladding was 6.55 mm and the inner diameter was 5.65 mm.

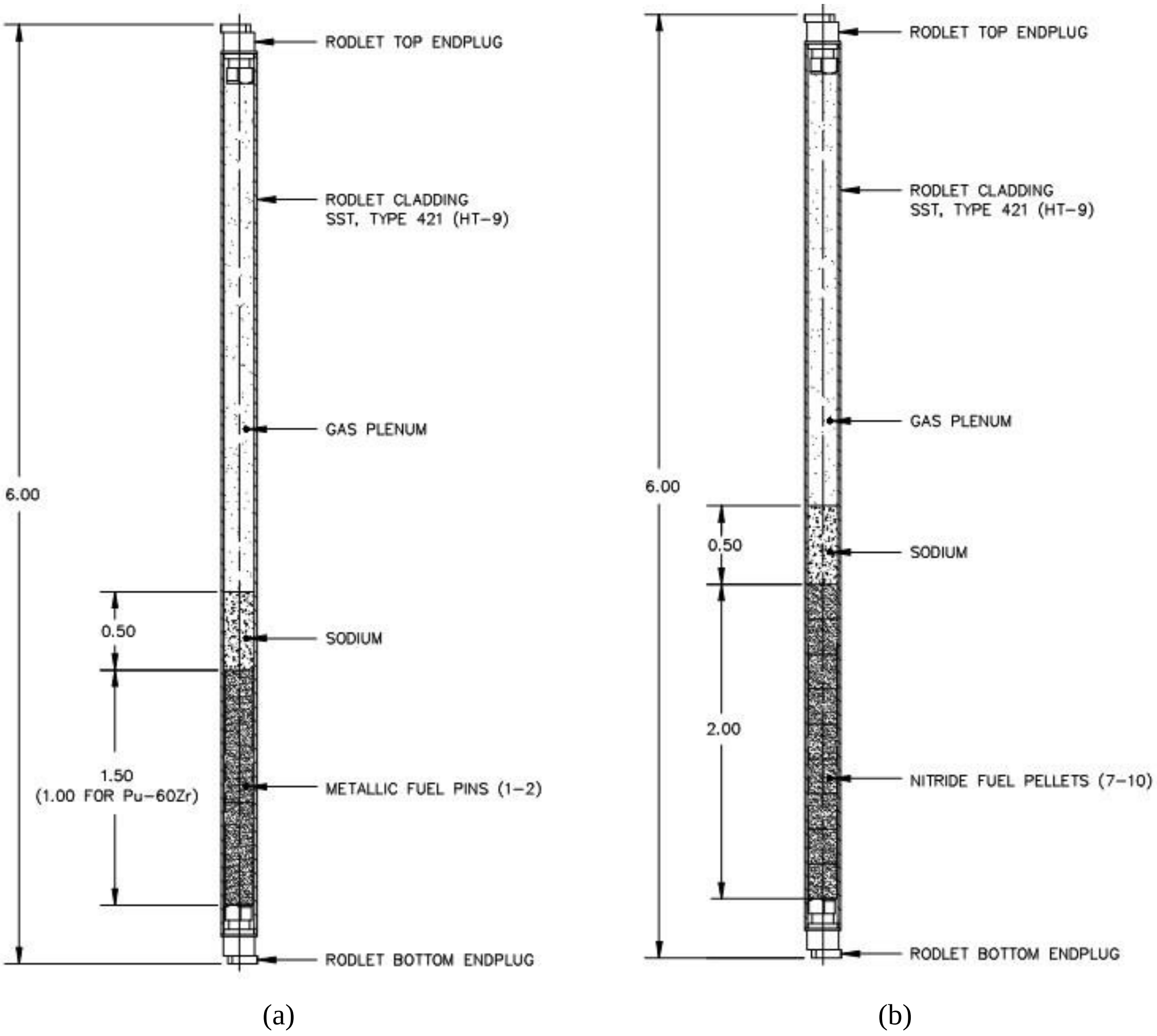

Figure 11. Rodlet assembly axial dimensions (inches) for a) metallic fuel and b) nitride fuel (dimensions in inches). The outer diameter of the cladding was 5.84 mm and the inner diameter was 4.95 mm.

Table 4. Key Irradiation Data Calculated from Simulations for FUTURIX-FTA (DOE1, 2, 3, 4) and Sister Pins from AFC-1 [13, 14, 26, 27]

Fuel	Fission density (f/cm3)	Burnup (at.% HM)	Av. LHGR (W/cm)	Peak temp cladding (°C)
DOE1	2.08 x 10^{21}	9.1	318	~ 550
AFC-1H: 1, 4	2.79, 3.91 x 10^{21}	18.01, 26.68	176, 248	~ 400, 495
DOE2	2.01 x 10^{21}	15.5	410	~ 545
AFC-1D: 1, 4	1.96, 2.84 x 10^{21}	15.68, 22.59	134, 193	~ 350, 430
AFC-1G: 1, 4	2.04, 2.98 x 10^{21}	14.07, 20.26	131, 192	~ 350, 425
DOE3	4.50 x 10^{20}	1.6	370	~ 520
AFC-1G:3	3.35 x 10^{21}	16.9	262	~ 490
AFC-1Æ: 6	4.50 x 10^{20}	3.5	218	~ 480
DOE4	4.08 x 10^{20}	4.1	280	~ 520
AFC-1Æ: 1, 3, 4	2.70-3.50 x 10^{20}	3 - 6	109, 150, 167	~ 310, 360, 390

3.1.1 Neutron Radiography

Neutron radiography was performed using the Neutron Radiography Reactor (NRAD) located in the basement of HFEF. The NRAD reactor is a 250kW TRIGA reactor with two beam lines. The east beam line services a position below the main floor of the hot cell and is used for irradiated fuel. Neutrons pass through the through the fuel specimen and expose different activation foils. The radiography fixture contains a scale marked with Gd paint that produces a calibrated scale for quantitative measurements of irradiated fuel dimensions.

Neutron radiography images were taken of the FUTURIX-FTA pins at 2 angles with both a dysprosium (Dy) foil for thermal neutron radiography and a Cd-covered indium (In) foil for epithermal neutron radiography. An example of the thermal neutron radiography with each pin labeled and demonstrating the spacing of the pins is shown in Figure 12. Detailed neutron radiographs of the fuel material are shown in Figure 13 for thermal neutron radiography and Figure 14 for epithermal neutron radiography.

As observed for the metallic fuel pins, the fuel has begun to creep down into the void space associated with the bottom endplug (which is normal), but there is no evidence of lift-off (which is sometimes observed). The bond sodium above the fuel appears to be free of any dissolved fuel material. It is possible to see some gaps between fuel slugs that generally correspond to the original fuel slug dimensions. This indicates very little axial growth in these fuel slugs. There is some enhanced neutron attenuation in the epithermal image in the central region of DOE2 (Pu-12Am-40Zr) that may indicate some constituent redistribution has occurred. The neutron radiography of the nitride fuel pellets (DOE3, DOE4) reveals the pellets maintained their geometry fairly well during irradiation and appear, overall, to have performed well. Some pellet chips can be observed in the neutron radiographs, but these chips are not unexpected since the as-fabricated nitride pellets were somewhat poorly consolidated and friable.

The performance of the FUTURIX-FTA nitride fuels, as indicated in the neutron radiographs, appears better than some of the corresponding nitride fuels irradiated in the ATR (AFC-1Æ and AFC-1G). It should be noted that the appearance of the fuels in the neutron radiography of AFC-1Æ rodlets 1, 4 and 6 appear remarkably similar to the radiography of FUTURIX-FTA (DOE3 and DOE4) [13, 21].

The neutron radiography from the low-fertile metallic fuels in AFC-1H are shown in Figure 15 for thermal neutrons and Figure 16 for epithermal neutrons. As with the FUTURIX-FTA radiographs, it is possible to see some separation between fuel slugs, especially in AFC-1H R1 (this is not uncommon and happens during postirradiation transportation and handling when a metallic fuel pin is not maintained in a vertical position at all times). There appears to be a small amount of material dissolved in the bond sodium above the fuel column and what appears to be a void in the center of AFC-1H R1. Likewise, the applicable non-fertile metallic fuel rodlet neutron radiography from AFC-1D and AFC-1G are shown in Figure 17 for thermal neutrons and Figure 18 for epithermal neutrons. As with AFC-1H R1 it is possible to see separation between constituent fuel slugs in AFC-1D R1. There does appear to be some highly swelled, less dense fuel material at the top of some of these fuel columns. The thermal neutron radiography from the AFC-1 nitride fuels that are applicable to FUTURIX are shown in Figure 19 for the low-fertile composition and Figure 20 for the non-fertile composition. It should be noted that the thermal neutron radiography of the nitride fuel presented in these figures is a composite of rodlet and capsule neutron radiography. There appears to have been some handling damage occur to AFC-1Æ during PIE between capsule and neutron radiography. In Figure 19 and Figure 20 AFC-1Æ R1, R3, & R6 are shown from capsule neutron radiography and AFC-1G R3 and AFC-1Æ R4 are from rodlet neutron radiography.

In general, the fuel conditions observed in the neutron radiography of the Phénix-irradiated FUTURIX-FTA fuels and the AFC-1 fuels irradiated in cadmium-filtered positions in the ATR is qualitatively similar. The most notable exception is the high neutron attenuation in the epithermal neutron radiography along the central axis of DOE2 that is not seen in the AFC-1D or AFC-1G data.

The quantitative measurement generally obtained from neutron radiography of irradiated fuels is axial growth of the fuel column. For EBR-II metallic fuel experiments, axial growth of the fuel slug was mostly easy to measure using neutron radiography or precision gamma scanning. The fuel slugs began irradiation at 34.3 cm long and although the fuel sometimes looked much less dense at the top and making identifying the exact point of the top of the fuel slug difficult, the fuel axial growth data obtained in this way was generally consistent. In contrast, the fuel segments in the ATR experiments are less than 4 cm long and often exist in several segments, three in the case of AFC-1H rodlet 1 and AFC-1D rodlet 1. (see Figures 9 and 11a). This makes it very difficult to assess in a consistent way the axial growth in these short fuel column rodlets to compare to EBR-II experiments or even to FUTURIX-FTA (which had fuel columns of 10 cm). There is simply too much subjective judgment in selecting the as-irradiated fuel slug length, so comparison to axial growth measurements from EBR-II or even to FUTURIX-FTA is not meaningful. Furthermore, there is a lack of consensus among experts concerning how to understand the phenomenon of axial growth in metallic fuels. There is some evidence that suggests axial growth in metallic fuel may be in part an end effect that happens in close proximity to the unconstrained, free fuel surface at the top of the fuel column. For example, measured axial growths in FFTF irradiations of metallic fuel have been noted to be less than those for identical compositions in EBR-II [28]. If that is the case, it may not make sense to compare axial growth expressed as a percent of total fuel length for metallic fuel columns of significantly different lengths. This may not be a fuel phenomenon that necessarily differs solely due to differences in neutron spectra, but differs in part due to differences in total fuel length. For this reason, quantitative measurements of axial growth in the metallic fuels of FUTURIX-FTA versus the cadmium-filtered AFC-1 tests is not a reliable fuel performance phenomenon that can inform the neutron spectrum comparison that is the subject of this report.

Figure 12. Thermal neutron radiograph showing vertical spacing of FUTUTRIX-FTA fuel stack.

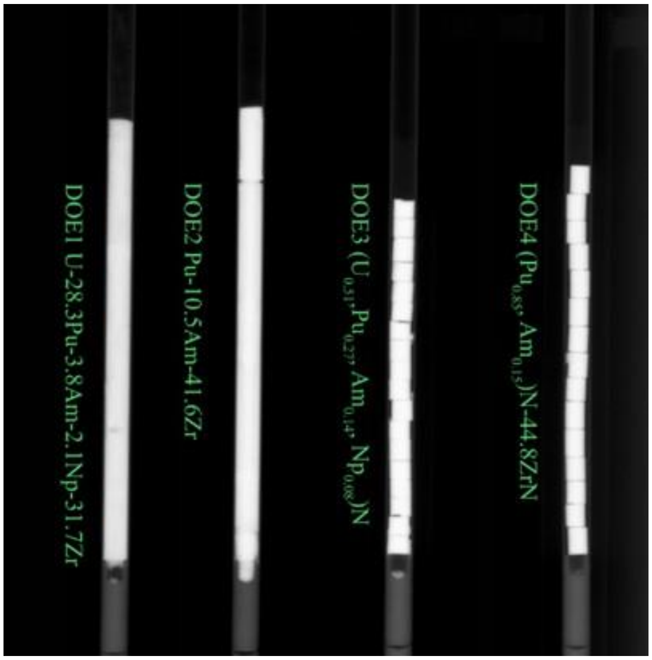

Figure 13. Thermal neutron radiography fuel material detail.

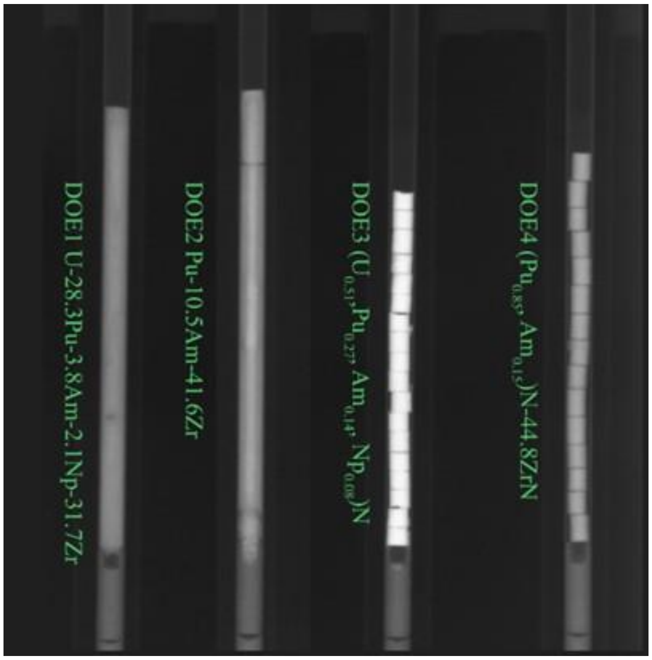

Figure 14. Epithermal neutron radiography fuel material detail.

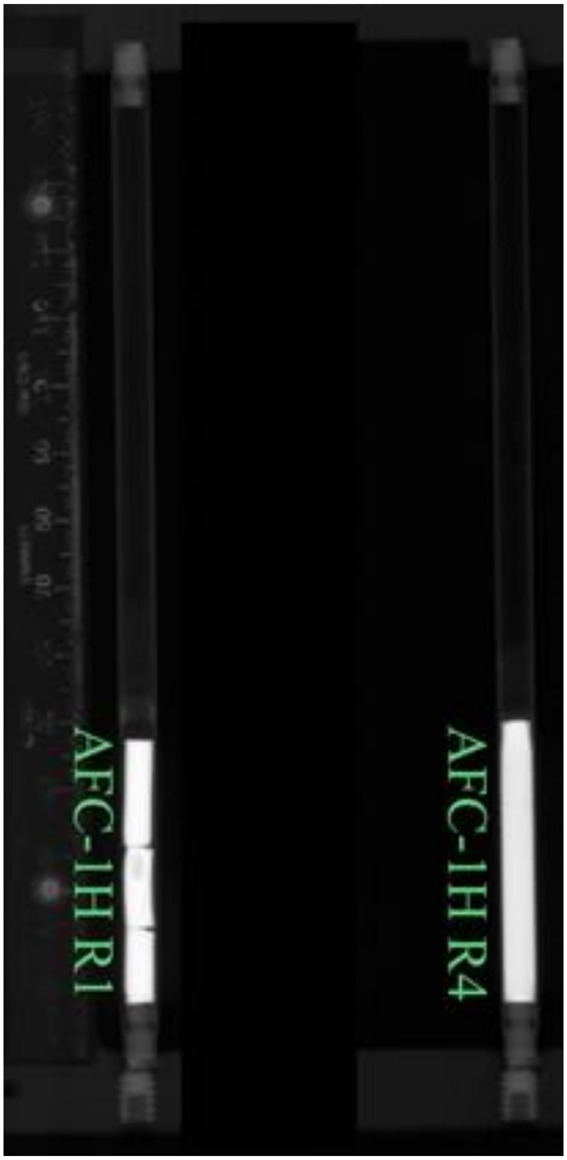

Figure 15. Thermal Neutron Radiography of Low Fertile metallic AFC-1 Rodlets.

Figure 16. Epithermal Neutron Radiography of Low Fertile metallic AFC-1 Rodlets.

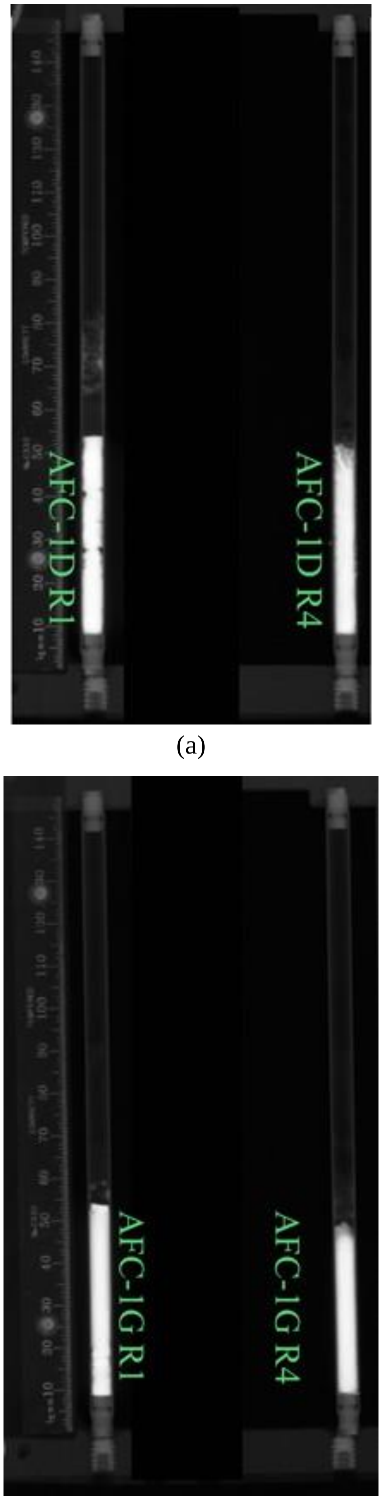

(a)

(b)

Figure 17. Thermal Neutron Radiography of Non-Fertile metallic AFC-1 Rodlets (a) AFC-1D rodlets (b) AFC-1G rodlets.

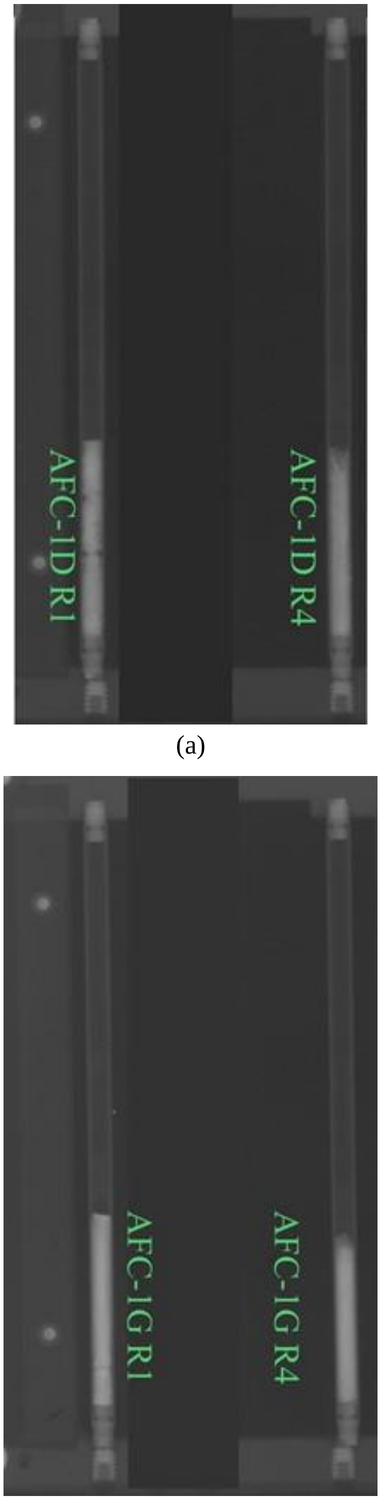

(a)

(b)

Figure 18. Epithermal Neutron Radiography of Non-Fertile metallic AFC-1 Rodlets (a) AFC-1D rodlets (b) AFC-1G rodlets.

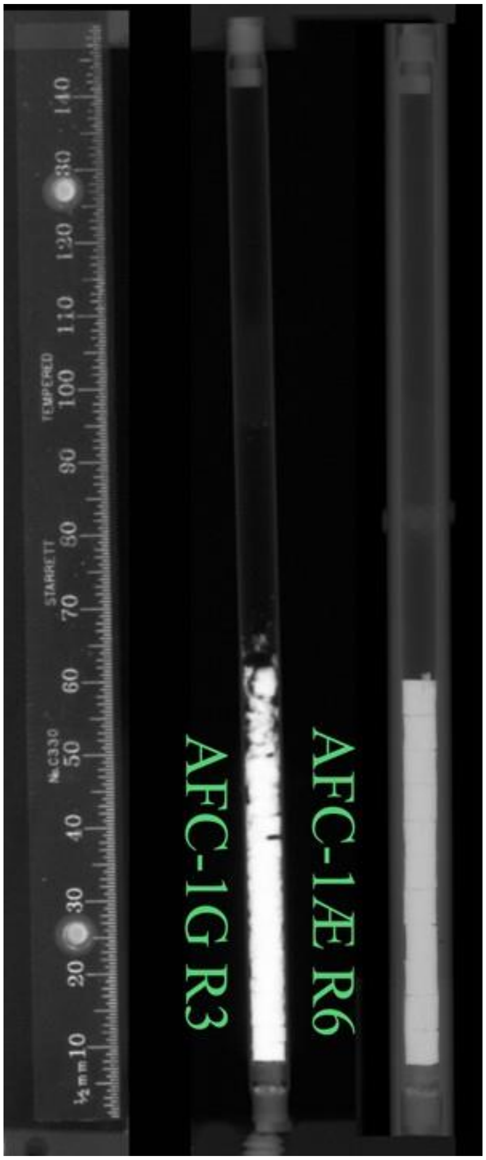

Figure 19. Thermal Neutron Radiography of Low Fertile Nitride AFC-1-Rodlets.

Figure 20. Thermal Neutron Radiography of Non-Fertile Nitride AFC-1 Rodlets.

3.1.2 Dimensional Inspection

Dimensional inspections of FUTURIX-FTA rodlets was performed using the HFEF contact profilometer. Outside diameter measurements were collected all along the rodlets in roughly 0.127 cm increments and at 6 angles spaced 30° apart. Diameter measurements are collected with ±0.0005 cm accuracy. The diameter measurements were performed prior to the removal of the extensions and it is possible to ascertain the beginning and end of the rodlets by diameter spikes associated with the welds on the extensions and rodlet endcaps. Given the accuracy of the instrument, no perceptible strain was detected in any of the 4 FUTURIX-FTA rodlets. In the metallic fuel pins where fuel was present, there may have been a diametral strain of 0.1%, but this strain is at the limit of the instrument uncertainty. Diametral strain was calculated based on the as-fabricated diameter of the AIM-1 cladding which is 6.565 mm. The measured diametral strain is shown in Figure 21, Figure 22, Figure 23, and Figure 24 for DOE1, DOE2, DOE3, and DOE4 respectively. The strain peaks indicate the locations of welds where the rodlets are attached to endcaps and extensions. The rodlets profiles are shown with the plenum to the left and fuel zone to the right. The uncertainty shown for each measurement is 7.7×10^{-4}, which is the 1-sigma uncertainty. Thus, while there is a consistent strain indicated in the fuel zone of DOE1 and DOE2, indicating some effect. This strain is at the limit of the sensitivity of the HFEF element contact profilometer.

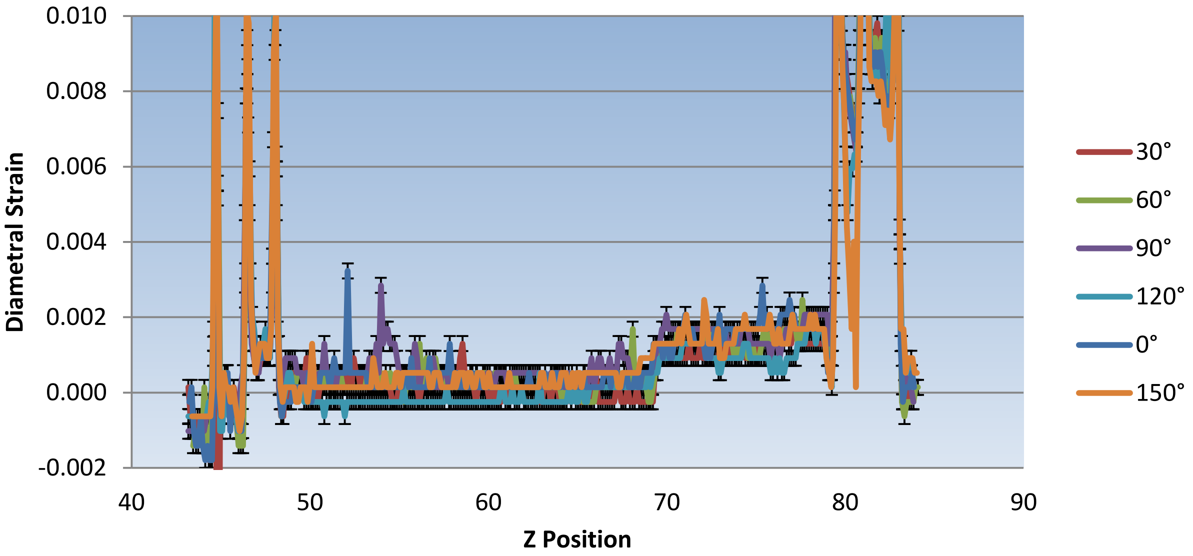

Figure 21. Diametral cladding strain measured for DOE1 (low-fertile metallic).

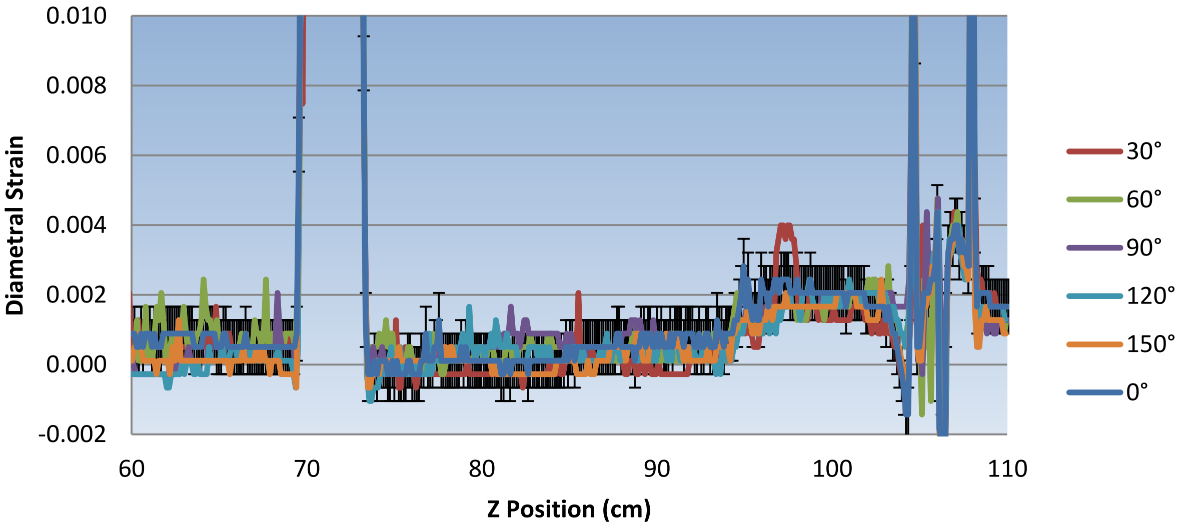

Figure 22. Diametral cladding strain measured for DOE2 (non-fertile metallic).

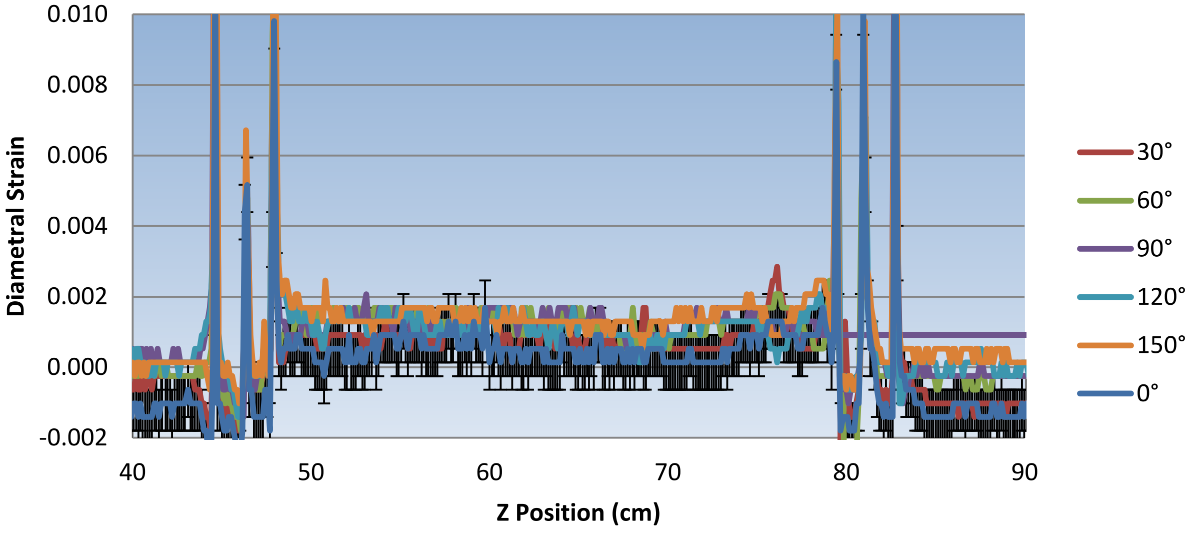

Figure 23. Diametral cladding strain measured for DOE3 (low-fertile nitride).

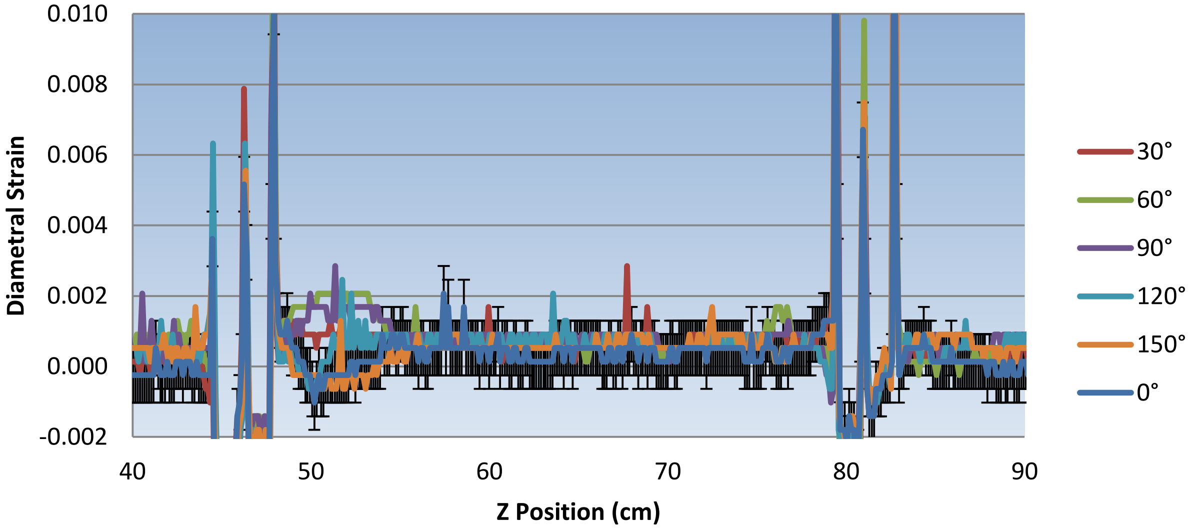

Figure 24. Diametral cladding strain measured for DOE4 (non-fertile nitride).

For the AFC-1 rodlets with metallic fuels, the diameter profile measurement was obtained with the Remote Fuel Metrology System at HFEF (designed specifically for the short rodlets used in the AFC test series). Axial cladding profilometry was collected to record diameter data at axial positions between 10.2 to 142.2 mm (0.4 to 5.6 in., with respect to the bottom of the rodlet) at intervals of 1.27-2.54 mm (0.050-0.100 in.). Four axial scans, 45 degrees apart (0°, 45°, 90°, 135°), were recorded for each rodlet. The uncertainty of the diameter measurement is ±0.0076 mm (±0.0003 in.). The accuracy of the diameter measurement is validated at the beginning of a series of measurements, and at the beginning and ending of each shift of operation during an extended period of use.

The dimensional data collected for the AFC-1 metallic fuel rodlets can be found in Reference 13. The dimensional data show no uniform diameter increase in any areas of the rodlets at all collected angles. There were several spikes at random axial positions and azimuthal rotations in the collected data that have been attributed to contamination or debris from capsule disassembly on the surface of the rodlets. The nitride bearing AFC-1Æ and AFC-1G rodlets that are applicable to FUTURIX-FTA were all evaluated for dimensional changes. However no change in dimensions was observed. Because no changes were observed, the AFC-1 data is not shown in this report. The lack of any measurable diametrical strain is expected for the AFC-1 rodlets. The cladding temperature for the AFC-1 rodlets was lower than FUTURIX-FTA (see Table 4), and no strain would be expected at these irradiation conditions.

3.1.3 Gamma Spectrometry

Gamma ray spectrometry of all of the AFC-1 and FUTURIX-FTA rodlets was performed using the HFEF Precision Gamma Scanner (PGS). However, major improvements occurred in the quality of the detector system and in the methodology of collecting gamma spectrometry data between the AFC-1 PIE campaigns and the FUTURIX-FTA PIE campaign. The raw spectra for the higher burnup AFC-1 irradiations (D, H, G) were recovered and reanalyzed as part of the present comparison activity, as much as was possible. However, the raw spectra were not available for the lower burnup AFC-1 irradiations. The quality of gamma spectrometry data produced for the AFC-1Æ irradiation is not acceptable for use and has not been reproduce here.

The PGS has three major components: collimator, stage, and detector. The collimator penetrates the HFEF cell wall with a rectangular aperture that is adjustable from 0.254 cm to 0.00254 cm in height and is 2.2225 cm wide. The collimator can be rotated from a horizontal to vertical orientation. The stage manipulates the sample in front of the collimator in the plane facing the collimator and can rotate the sample about its central axis. The detector consists of a Compton suppressed high purity germanium detector, and its control system moves the stage and collimator and initiates the scans.

Gamma spectrometry was performed on each FUTURIX-FTA rodlet individually. The plenum portion of the rodlet was scanned in 0.254 cm steps, and the fueled section of each rodlet was scanned in 0.127 cm steps for a live time of 30 minutes. A strong gamma-ray signal was also detected from Cm-243, which is likely due to the significant initial Am content in the fuel. It is possible to ascertain information about Cm and Am distribution in the fuel from this signal. A representative gamma ray spectrum from DOE1 is shown in Figure 25. In this figure, the Cm-243 signal is highlighted. Several fission products were also detected in the gamma spectrometry including: Ru-106 (as Rh-106), Sb-125, Cs-134, Cs-137, Ce-144, Eu-154, and Ce-144 (as Pr-144). Additionally, several activation products were detected, including Co-60 and Mn-54. Since Mn-54 is not a fission product, its signal is used in the axial profile plots to indicate the location of the cladding and cladding endcaps where this signal spikes.

A similar analysis was applied to the available data from AFC-1. In scanning the AFC-1 rodlets, the live time was considerably shorter (2 minutes) than for FUTURIX-FTA rodlets. The collimator slit width and step size was 0.127 cm. It was not possible to detect Cm-243 in the data collected from AFC-1.

The behavior of gamma emitting fission products appears to be similar between FUTURIX-FTA and its AFC-1 sister pins. In the metallic fuels (DOE1, DOE2, AFC-1H, AFC-1D, AFC-1G), Cs radioisotopes have been dissolved in the Na bond between the fuel and cladding, producing a Cs activity spike in the Na plug region above the fuel. This can be seen in Figure 26 and Figure 27 for FUTURIX-FTA, Figure 28, Figure 29, Figure 30, and Figure 31 for AFC-1H R1, AFC-1H R4, AFC-1D R1, and AFC-1D R4, respectively. The presence of Cs in the sodium plug above the fuel has historically been a good indication of rodlet integrity (since the pressurized gas plenum typically forces this sodium/cesium out of the fuel pin through any cladding breach in the fuel region). There are also Cs spikes present at the interface between different slugs used to create the DOE2 fuel stack. This is highlighted in Figure 27 with image overlays of the neutron radiography and the as-fabricated fuel slugs lining up with the Cs signal spikes at 89, 92 and 96 cm. Europium has also migrated into the Na bond and plug, and the measured activity trace of Eu-154 is shown in these figures for metallic alloy fuels. There is no evidence of significant rare earth (Ce) migration to the fuel periphery which might indicate unexpectedly high levels of fuel-cladding chemical interaction (FCCI). The relative level of Ce migration to the fuel periphery is measured by comparing the Ce-144 activity calculated by the 133.5 keV gamma-ray and the higher energy (696, 1489 and 2186 keV) gamma-rays from the daughter of Ce-144, Pr-144, that is in secular equilibrium with Ce-144. If the Ce-144 activity by the 133.5 keV gamma-rays rises relative to the Ce-144 activity by the 696 keV, 1489 keV, and 2186 keV gamma rays, it would indicate a higher amount of Ce-144 near the cladding, because the 133.5-keV gamma is less attenuated by the highly dense fuel. The Ru in these rodlets appears to be well integrated into the fuel as does the Cm-243. These trends are consistently repeated for all metallic fuel rodlets. For this reason, the AFC-1G metallic fuel gamma spectrometry is not shown. There does not appear to be any differences observed between FUTURIX-FTA and AFC-1 for the gamma spectrometry data collected for the metallic fuels, so the neutron spectrum differences did not apparently lead to macroscopic differences in distribution of fission products within the fuel rod.

The gamma spectrometry of the nitride fuels in FUTURIX-FTA (DOE3 and DOE4) reveals Cs migrating out of the fuel and depositing in the cooler sodium plenum as expected from thermodynamics. This is seen as small shoulders on the Cs distributions shown in Figure 32 and Figure 33. All other fission products appear to have been retained in the nitride fuel matrix. The Cm-243 signal in DOE4 was significantly lower than expected based on the nominal composition and the Cm-243 signal from DOE3. However, the atom density of Am is higher in DOE3 than DOE4, so the Cm-243 signals would seem to be consistent given the relative densities. The Cm-243 signal contains a great deal of statistical noise in DOE4 and is not plotted in Figure 33. As was the case in the metallic fuels, the Ru signal for the nitride fuels indicates that it and likely other noble metals (Ru, Rh, Pd, Mo, Tc) are stable in the fuel matrix.

As noted previously, the AFC-1Æ data was not adequate for interpretation, but the low-fertile nitride rodlet from AFC-1G R3 was analyzed and is presented in Figure 34. The trends present in this data set appear to be consistent with the FUTURIX-FTA data. There does appear to be a small amount of Cs dissolved in the sodium plug above the fuel column. The Ru appears to be collocated with the fuel, presumably inside the fuel matrix. In this rodlet, the neutron radiography is especially helpful in interpreting the gamma spectrometry due to the relocation of fuel fragments experienced during storage. As with the metallic fuels, there is no evidence of any differences between the axial distribution of gamma emitting radionuclides between the FUTURIX-FTA and the AFC-1 rodlets, although there is admittedly considerably less data available for consideration for the nitride fuels.

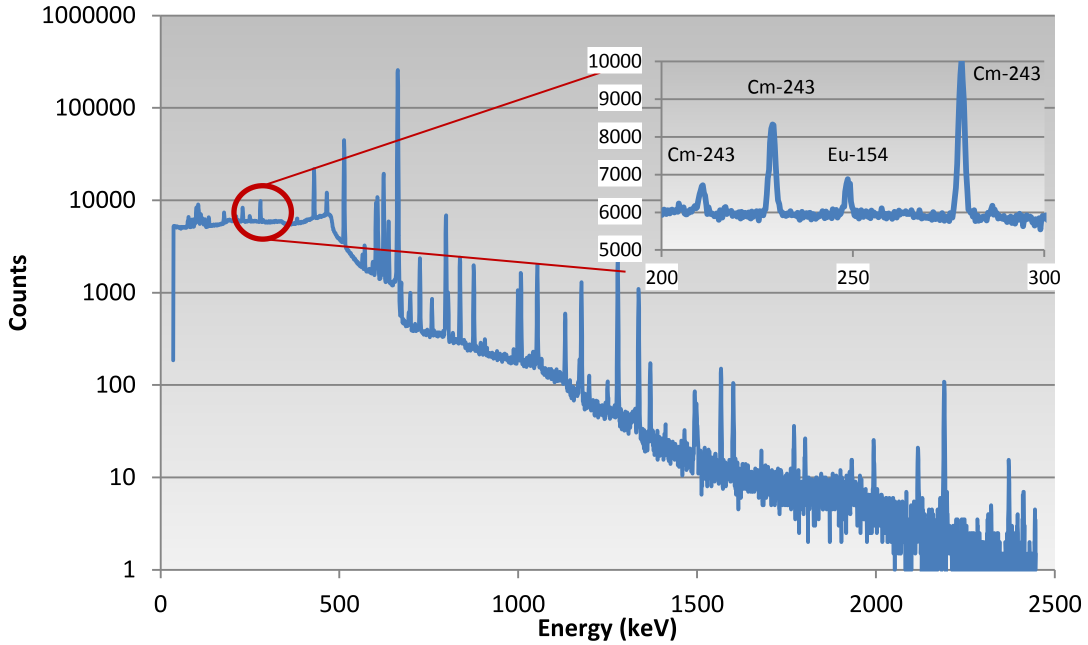

Figure 25. Representative gamma-ray spectrum from DOE1 (U-29Pu-4Am-2Np-30Zr. low-fertile metallic) fuel mid-plane with a detail of the spectrum corresponding to the Cm-243 signal.

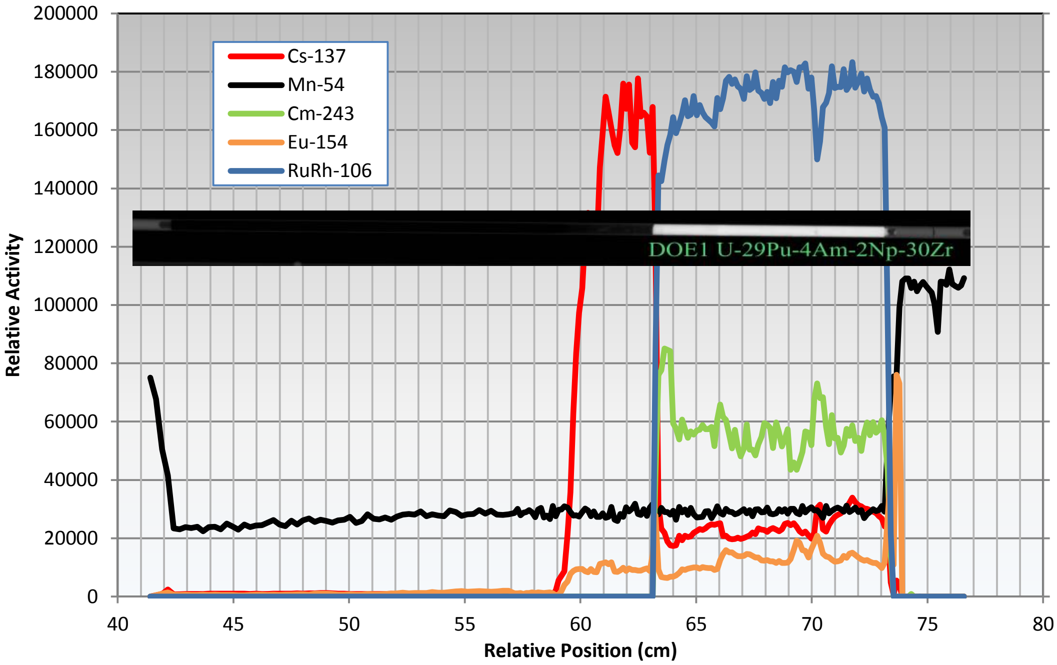

Figure 26. Axial distribution of select gamma emitting radionuclides in FUTURIX-FTA DOE1 (low-fertile metallic).

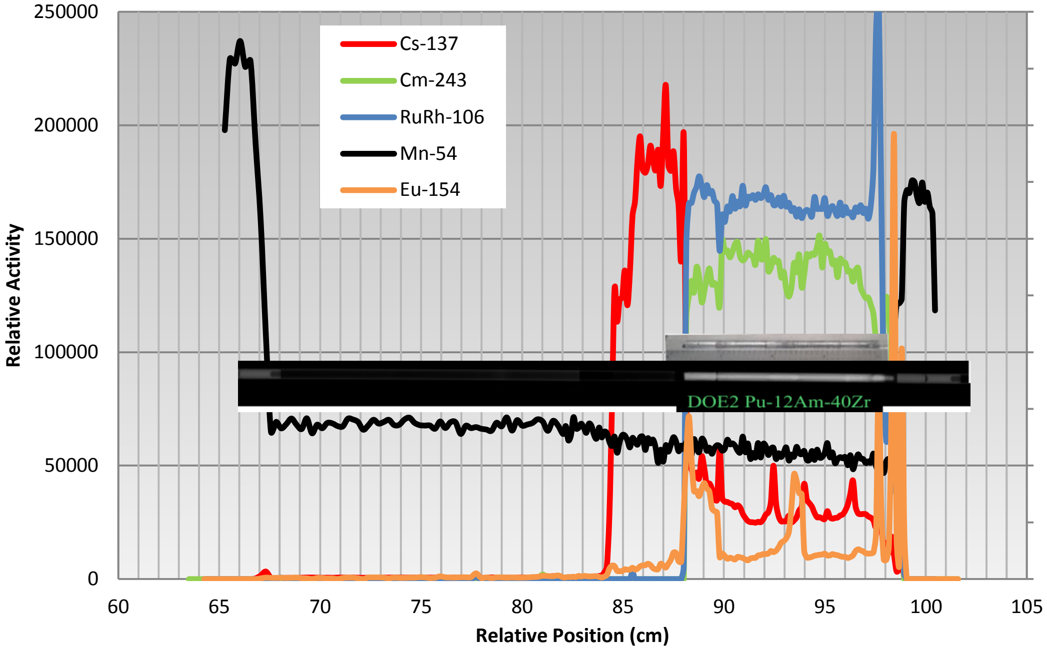

Figure 27. Axial distribution of select gamma emitting radionuclides in FUTURIX-FTA DOE2 (non-fertile metallic).

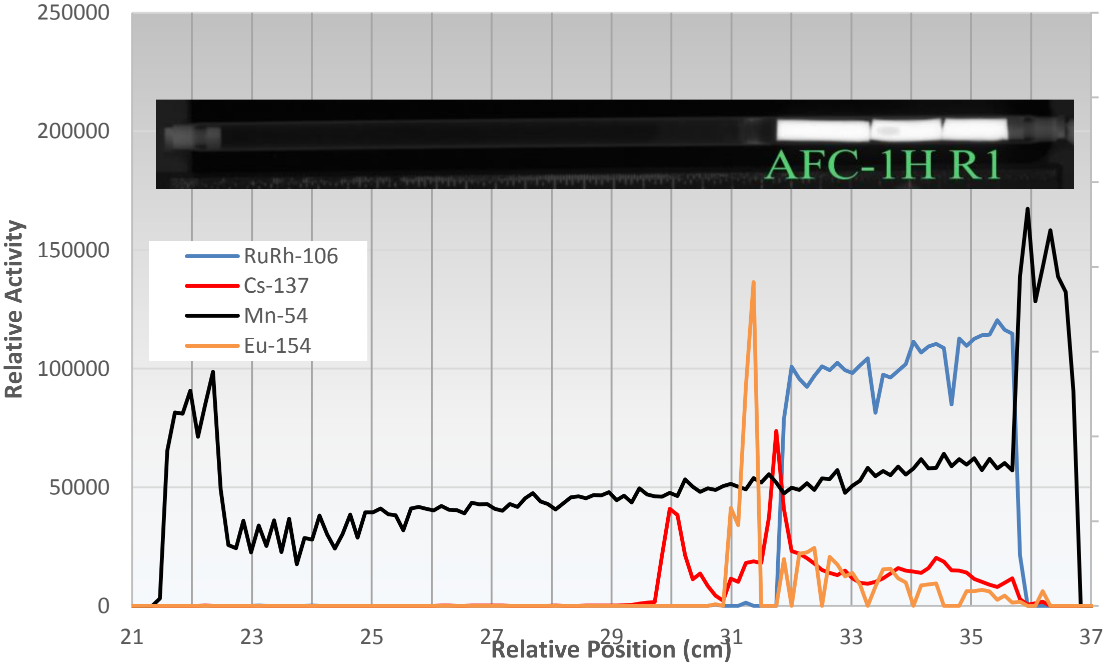

Figure 28. Axial distribution of select gamma emitting radionuclides in AFC-1H R1 (low-fertile metallic).

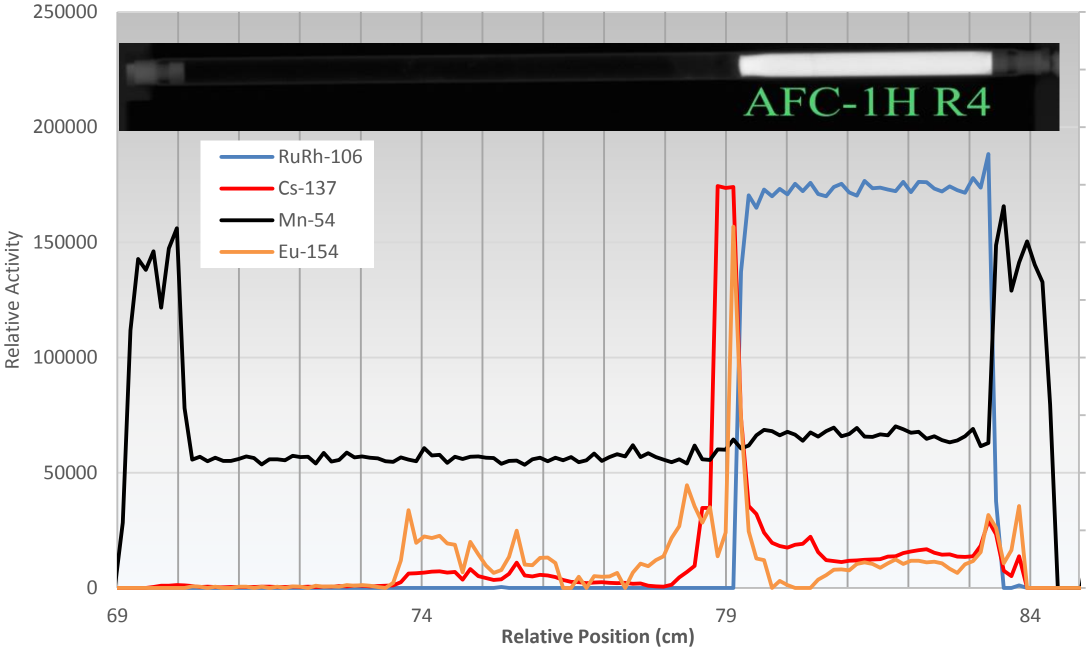

Figure 29. Axial distribution of select gamma emitting radionuclides in AFC-1H R4 (low-fertile metallic).

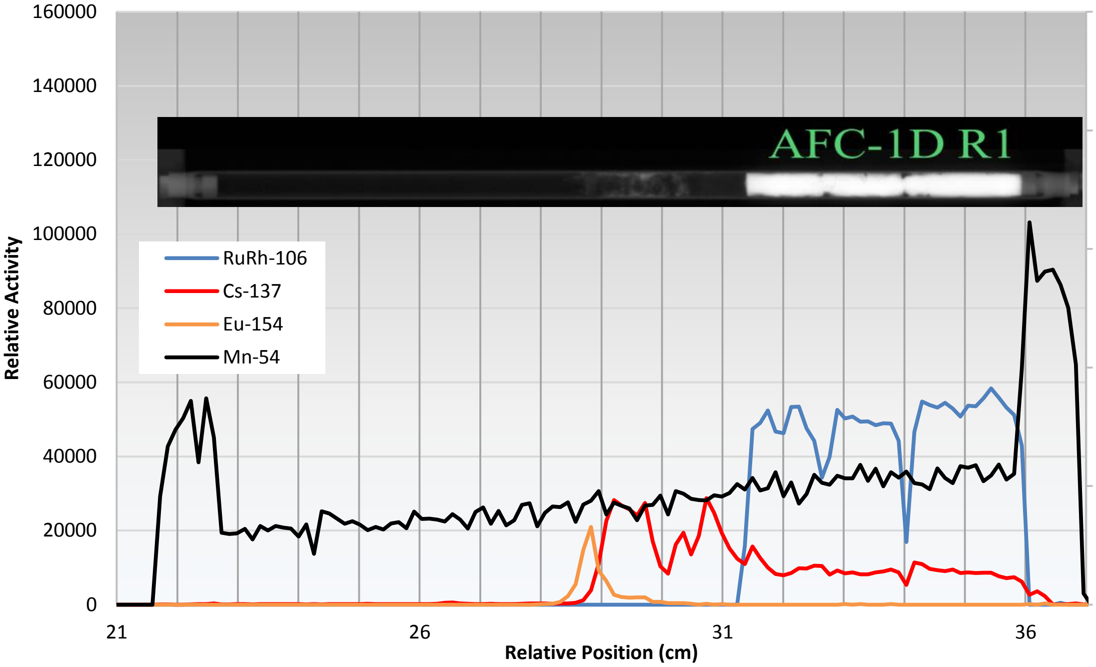

Figure 30. Axial distribution of select gamma emitting radionuclides in AFC-1D R1 (non-fertile metallic).

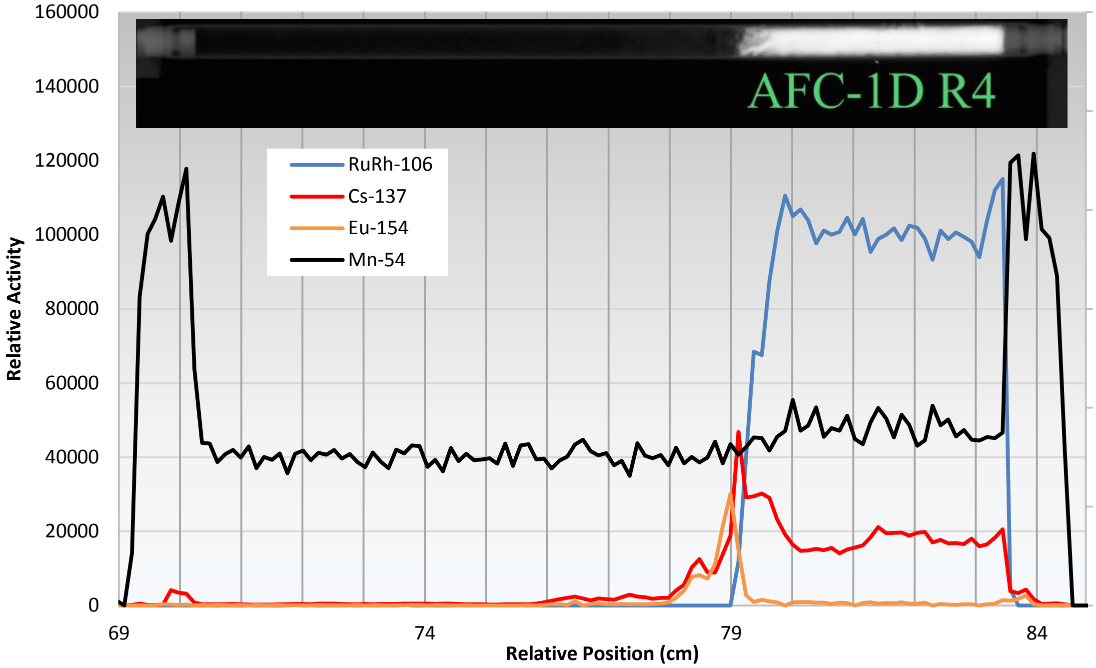

Figure 31. Axial distribution of select gamma emitting radionuclides in AFC-1D R4 (non-fertile metallic).

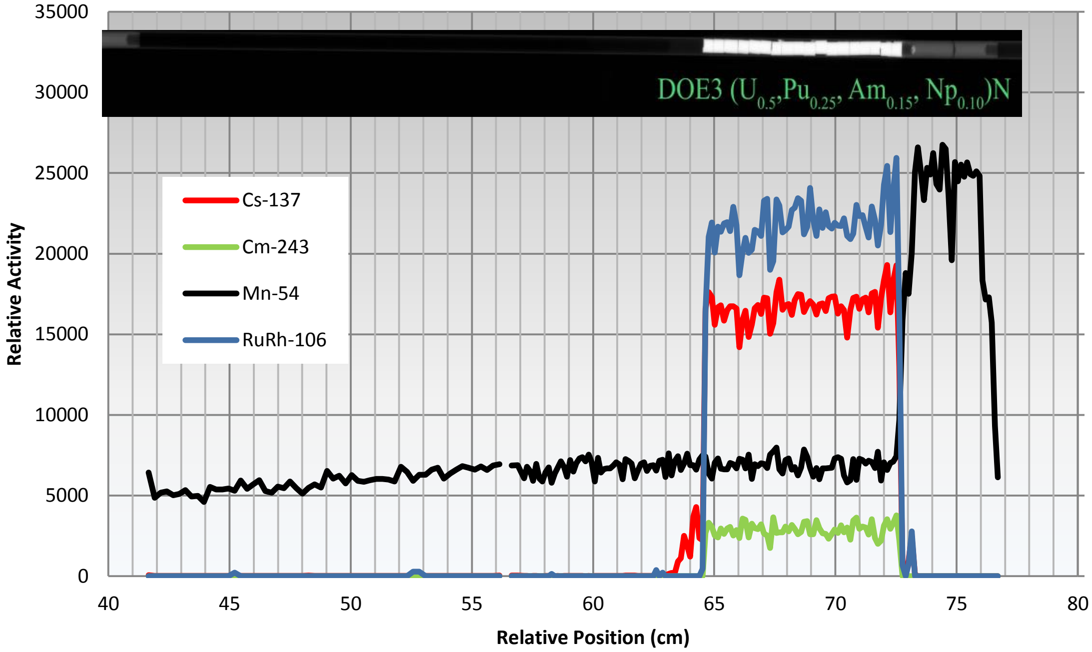

Figure 32. Axial distribution of select gamma emitting radionuclides in FUTURIX-FTA DOE3 (low-fertile nitride)

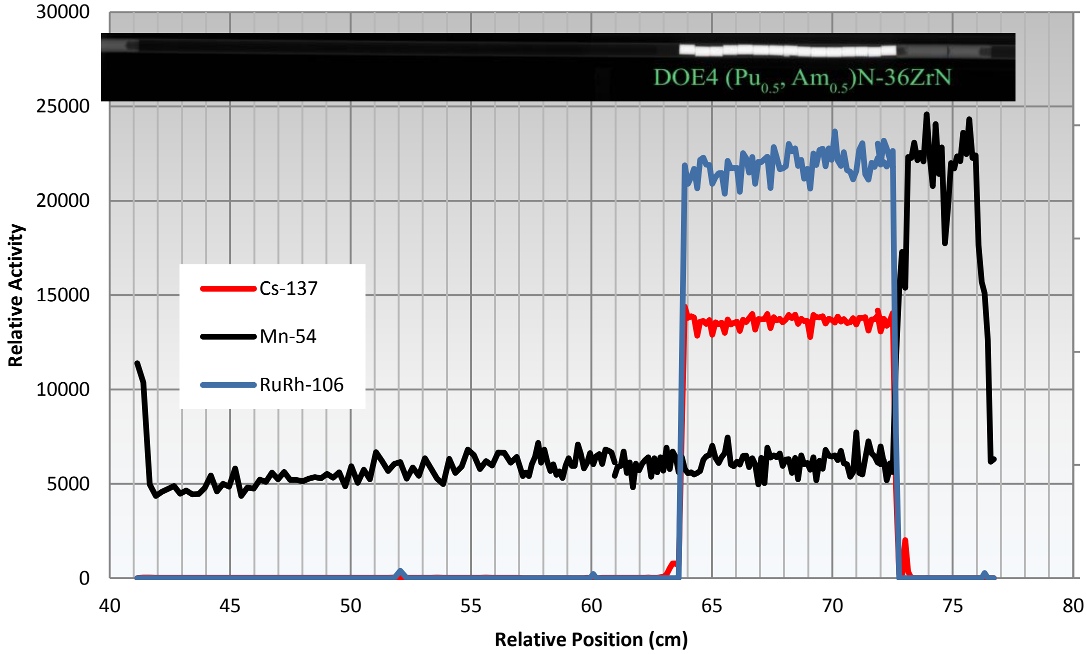

Figure 33. Axial distribution of select gamma emitting radionuclides in FUTURIX-FTA DOE4 (non-fertile nitride)

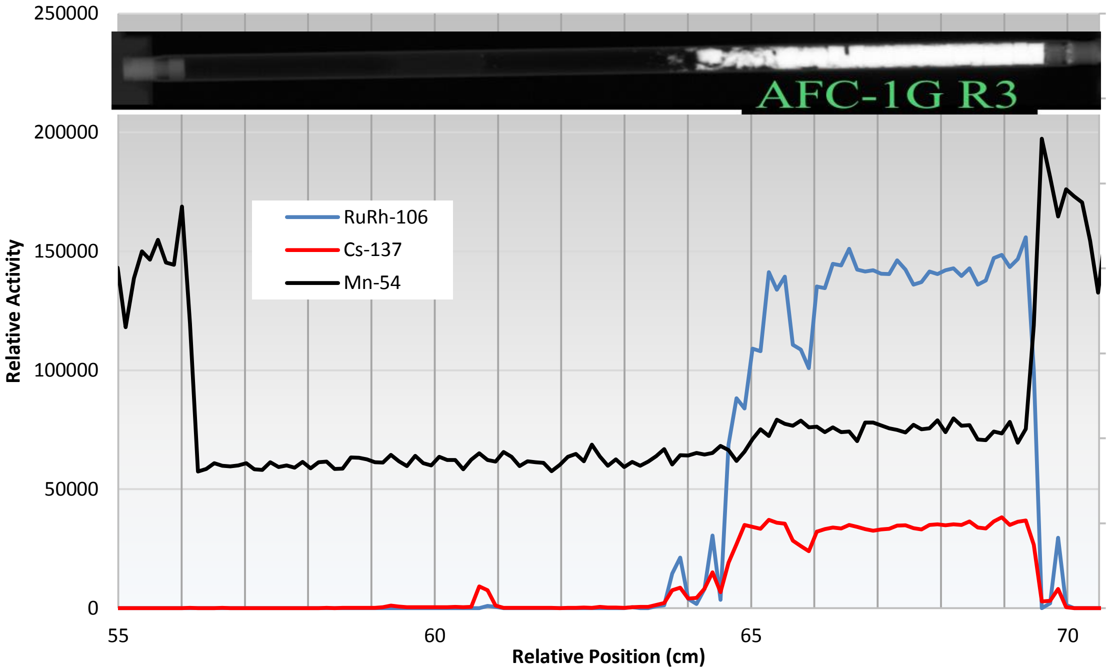

Figure 34. Axial distribution of select gamma emitting radionuclides in AFC-1G R3 (low-fertile nitride)

In addition to axial gamma spectrometry scans, it is possible to rotate the HFEF PGS collimator from a horizontal to a vertical orientation. In this orientation it is possible to move an axial level of the fuel past the collimator and perform a series of rotations over several angles. The resulting signals over several angles can be collected and tomographically reconstructed to provide a two dimensional distribution of fission products averaged over an axial location. This is referred to as Gamma Emission Computed Tomography (GECT). The full details of this technique are available in Reference 29 and the demonstration of this technique can be seen in Reference 30 and 31. This technique is similar to conventional X-ray computed tomography, but it is limited by the number of angles that can practicably be collected as spectrum collected takes several minutes and the total collection time can extend to several days or weeks for a fully characterized rodlet. Unfortunately, this technique was not implemented at HFEF until well after the AFC-1 PIE campaign had been concluded. GECT from FUTURIX-FTA is included here, since the data is useful in understanding the fuel performance of these alloys.

The GECT technique was applied to both DOE1 and DOE2 in 0.0254 cm steps over 16 equally spaced angles between 0 and 180°. For both rodlets, data was collected at the mid-plane of the fuel slug. The results of the GECT for Cs-137, Ru-106, and Cm-243 are shown in the Figure 35, Figure 36, and Figure 37, respectively, for both DOE1 and DOE2. The Cs-137 distribution is quite different for the two rodlets shown in Figure 35. Optical microscopy sheds some light on this behavior and is discussed in Section 3.1.6. In short, there was a great deal of open porosity in the interior of the fuel pin at this level. Cs produced by fission likely was dissolved in Na that migrated into the open porosity in this region of the fuel. In the past, a similar Cs spike was also observed in the interior fuel. During the Integral Fast Reactor (IFR) program a punch electrical discharge machine (EDM) was used to look at several radial positions in irradiated U-20Pu-10Zr metallic fuel. When the samples were counted the Cs profile matched the distribution seen in Figure 35(a). However, at the time this result was viewed with skepticism and was not published [32]. Further investigation into this behavior might be warranted, as this behavior could have implications on how the thermal behavior of the fuel is modeled, and it may be possible to infer the extent of sodium logging present in a pin by this method. The Cs distribution in DOE2 appears to be in a ring around the fuel slug. This is the behavior typically seen in other metallic fuel [31]. This likely indicates Cs has migrated out of the fuel matrix and is in solution with the bond Na that remains between the fuel and the cladding. The distribution of Ru-106 for both DOE1 and DOE2 are similar and shown in Figure 36. The distribution appears to be a ring at the periphery of the swollen fuel slug, and the axial data suggests Ru-106 is stable in the fuel. A peripheral ring of Ru could be expected in the cadmium-filtered ATR rodlets, due to increased fission reactions occurring nearer the fuel periphery, but it is somewhat unexpected for rodlets irradiated in Phénix. The reduced level of Ru-106, and by implication lower fission rate, in the center of the rodlet may also have resulted from a significant Zr redistribution into the fuel center which is likely for DOE1 and DOE2 based on observed Zr redistribution behavior in metallic fuels from EBR-II [15]. Additionally for DOE1, the ring distribution of Ru-106 may also be indicative of the open porosity forming in DOE1 that was indicated by the Cs signal. Alternatively, the ring of Ru may be an indication of mobility above a certain temperature where the Ru is moving out of the hot central region of the fuel into the cooler periphery of the fuel, although such behavior from Ru has not previously been observed in metallic fuels.

The Cm-243 signal is shown in Figure 37, and this result is also difficult to interpret. The signal strength from DOE1 is not excellent, but generally appears to be a fairly constant distribution across the fuel. Local variations in Figure 37 are likely due to statistical variations in the collected spectra. The signal from DOE2 indicates a ring where no Cm-243 is located. This may suggest some chemical migration in the fuel that has shifted the Am or Cm concentration away from the mid-radius of the fuel. Future electron probe micro-analyzer (EPMA) investigation will likely be needed to confirm this observation.

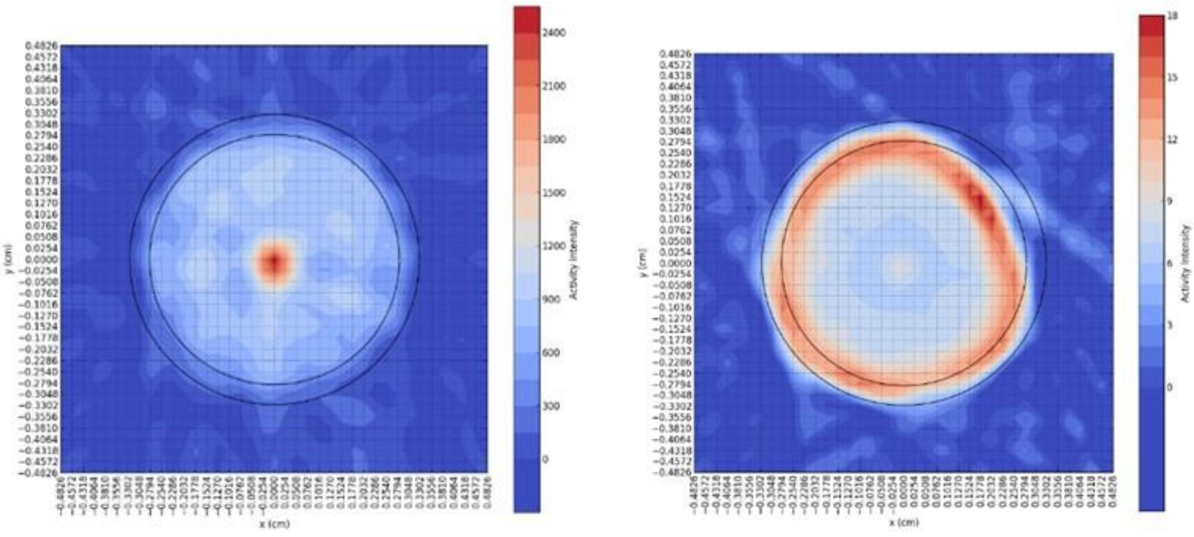

(a) (b)

Figure 35. Cs-137 Distribution in the middle of the fuel zone for DOE1 (low-fertile metallic) (a) and DOE2 (non-fertile metallic) (b).

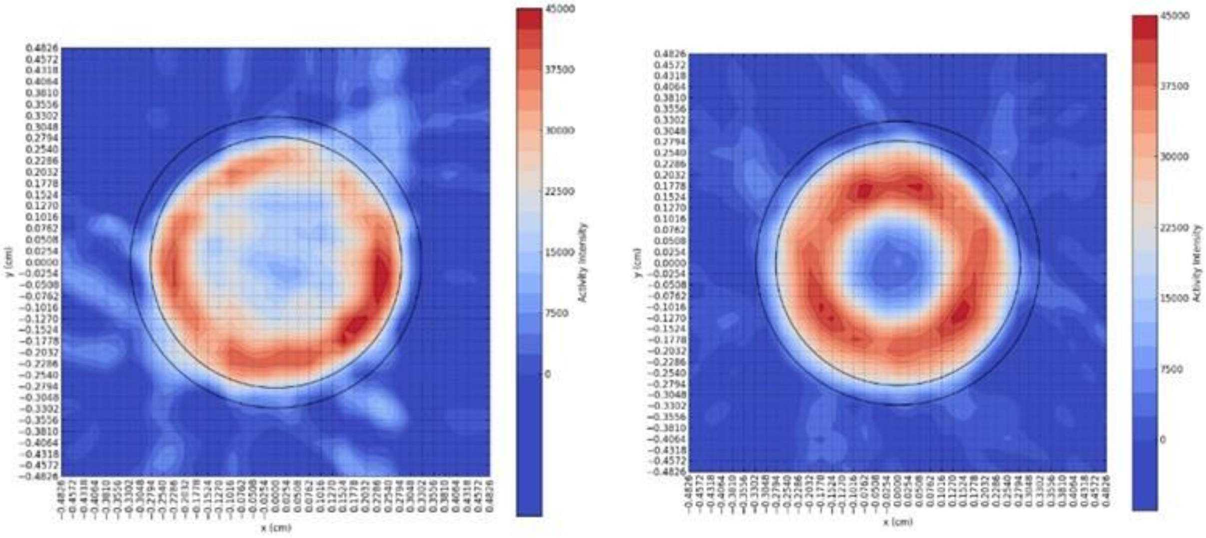

(a) (b)

Figure 36. Ru-106 Distribution in the middle of the fuel zone for DOE1 (low-fertile metallic) (a) and DOE2 (non-fertile metallic) (b).

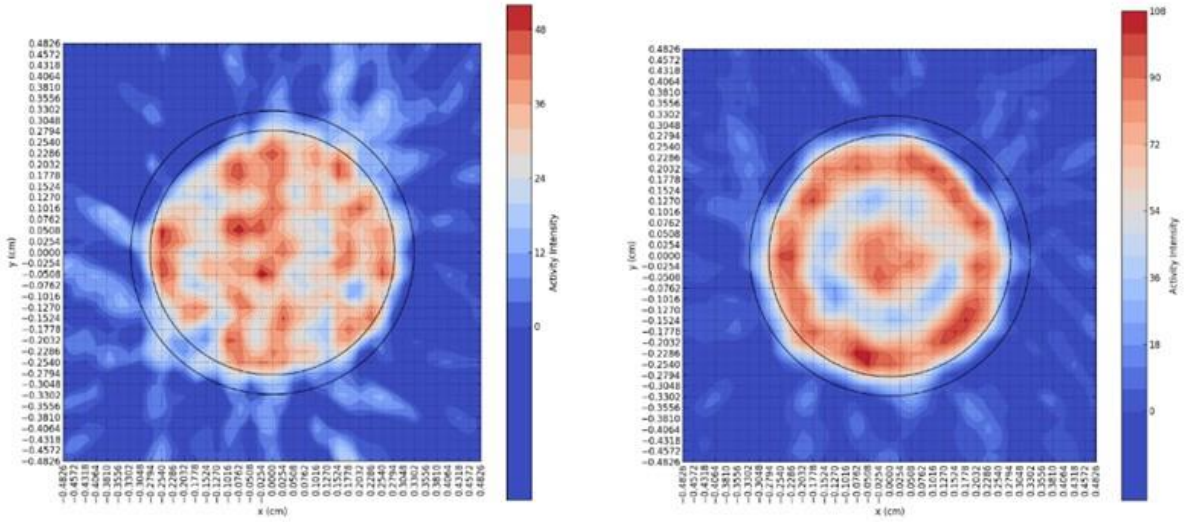

(a) (b)

Figure 37. Cm-243 Distribution in the middle of the fuel zone for DOE1 (low-fertile metallic) (a) and DOE2 (non-fertile metallic) (b).

3.1.4 Fission Gas and He Release

Fission gases were collected from the rodlets using the HFEF Gas Assay, Sample, and Recharge (GASR) system. Rodlets were punctured using a 150 W Nd-YAG laser system, and a gas sample was collected in a stainless steel bottle external to the hot cell. Void volume in the rodlet was then determined by a series of backfills into the punctured rodlet and expansions into the GASR system. The rodlet internal gas pressure was derived from the void volume measurement and the initial gas pressure measurement upon puncture. Fission gas analysis was performed by gas mass spectrometry. Results of fission gas analysis provided total elemental composition, krypton isotopic composition, and xenon isotopic composition. A summary of results for FUTURIX-FTA and AFC-1 sister rodlets is shown in Table 5. The combined Kr and Xe release is based on an estimate of the number of fissions that occurred in each rodlet from U-235, Pu-239 and other nuclei that is input into an empirical relationship between fission and atoms of Xe and Kr produced. The number of fissions in each rodlet was determined from ICP-MS The combined Kr and Xe release is based on an estimate of the number of fissions that occurred in each rodlet from U-235, Pu-239, and other nuclei that is input into an empirical relationship between fission and atoms of Xe and Kr produced. The number of fissions in each rodlet was also determined from ICP-MS results discussed in Section 3.1.5.

The FUTURIX-FTA rodlets were welded in a 75% Ar, 25% He gas mixture [33]. The total number of moles of gas present in the plenum can be calculated from the plenum pressure and the plenum volume using the ideal gas law. The PIE amount of Ar was compared to the expected amount of Ar in the pin from fabrication, and the two values were found to agree within less than 4%, indicating good samples were collected by GASR without any contamination from the argon atmosphere in the HFEF hot cell.

Compared to historic norms, the resulting fission gas releases are reasonable for the FUTURIX-FTA pins. A similar analysis was performed to derive fission gas release for the AFC-1 rodlets. The metallic fuel fission gas release is close to 70%±10% fission gas release that is typical of 75% smeared density U-Pu-Zr fuel behavior beyond ~5 atom % burnup [34]. The release value for DOE 1 is a little low compared to literature, but some of the AFC-1H pins with similar compositions and fission densities also had Kr+Xe releases between 50 and 60% [13]. It is not clear why the fission gas release in AFC-1H R1 is anomalously low. It was suspected that the bond sodium may have resealed the laser-induced hole in the cladding during sampling, preventing a full release of the fission gas, which has been known to happen with these AFC rodlets that have very short plenum lengths. DOE2, AFC-1D R1 and AFC-1G R1 all agree very well. AFC 1D R4 was breached in reactor and the collected fission gas from AFC-1G R4 was greater than the expected amount of fission gas produced from fission.

The nitride fuel fission gas release is very low, which is expected for nitride fuels in general, and is further exacerbated by the very short irradiation time experienced by the nitride fuels. The AFC-1 fission gas releases are slightly higher than the FUTURIX-FTA releases, but both are at levels considered low for fission gas release where variability is known to be subject to considerable scatter.

The helium releases are also shown in Table 5. The helium releases for the FUTURIX-FTA rodlets were 62 and 64% for the metallic fuels and 3 to 6 % for the nitride fuels. The helium production comes primarily from alpha decays of the many minor actinides produced in this fuel during irradiation and must be considered in fuels fabricated with significant levels of minor actinides due to its non-negligible contribution to plenum pressure. Similar He release values were derived for the AFC-1 rodlets.

In general, the fission gas and helium release values from the FUTURIX-FTA fuels are in reasonably good agreement with values obtained for the AFC-1 fuels, especially when the considerable variation between identical fuels irradiated under identical conditions is acknowledged.

Table 5. Fission Gas Release Summary.

Rodlet	**Kr+Xe Gas Release (%)**	**He Gas Release (%)**
	Low-fertile Metallic	
DOE1	51.6%	62.4%
AFC-1H R1	3.9%	<0%
AFC-1H R4	77.8%	73.2%
	Non-fertile Metallic	
DOE2	69.3%	64.2%
AFC-1D R1	87.7%	71.3%
AFC-1D R4	Breached	Breached
AFC-1G R1	63.1%	68.5%
AFC-1G R4	>100%	88.9%
	Low-fertile Nitride	
DOE3	3.4%	3.4%
AFC-1Æ R6	11.0%	5.4%
AFC-1G R3	8.8%	11.3%
	Non-fertile Nitride	
DOE4	2.5%	6.6%
AFC-1Æ R1	0.6%	0.5%
AFC-1Æ R3	14.3%	8.53%
AFC-1Æ R4	1.9%	0.8%

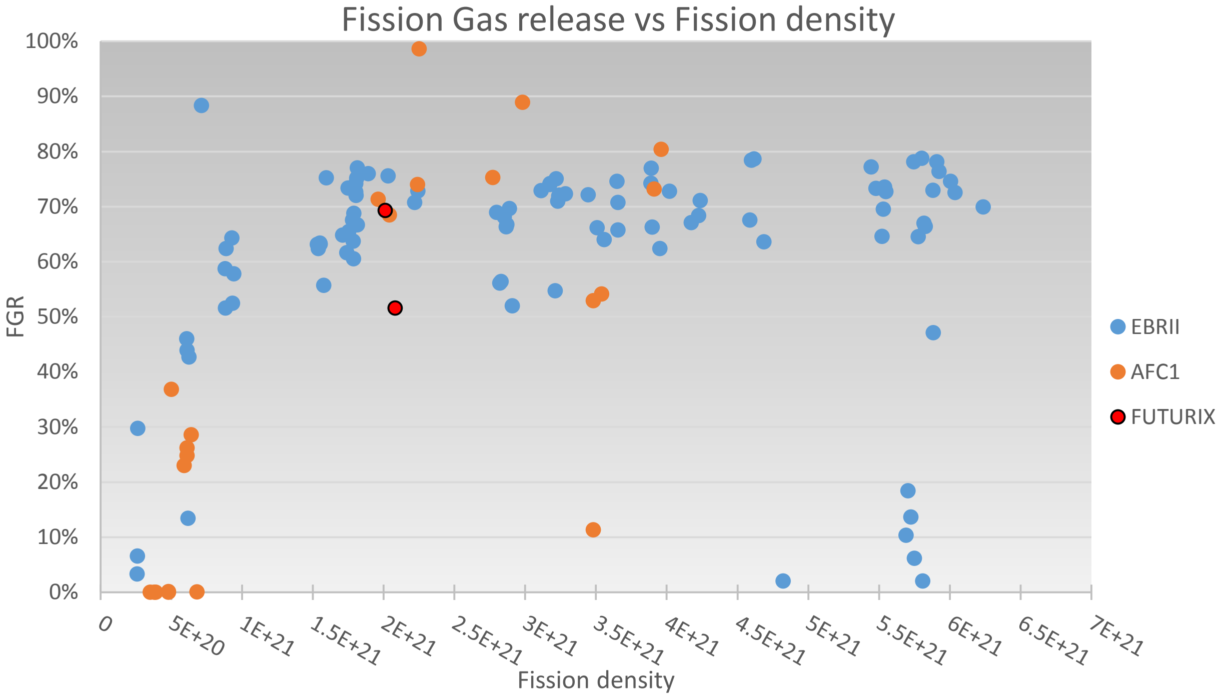

Figure 38. Fission gas release versus fission density for AFC-1, FUTURIX-FTA (metallic alloys), and the historic EBR-II database

3.1.5 Burnup/Transmutation

During rodlet sectioning to create the microscopy samples, additional samples were taken from near the fuel column mid-plane and sent to the INL Analytical Laboratory (AL) for a variety of chemical and isotopic analyses. The primary goal of these analyses was to ascertain the burnup of the sampled material. Gamma spectrometry analysis was also performed. Mass spectrometry analyses also provided information on the destruction/transmutation of the minor actinides. Minor actinide destruction is an essential goal of transmutation fuels.

Burnup is calculated from the results of mass spectrometry measurements of dissolved fuel samples. The methodology used to analyze FUTURIX-FTA and the AFC-1 rodlets is detailed in Reference 21. Briefly, the fuel is dissolved and aliquots are sent through several different inductively coupled plasma, mass spectrometry (ICP-MS) devices. A chemical separation for Pu was performed to help fully analyze the actinide content of the fuel. The determination of burnup was performed using the measured mass of a specific fission product in the fuel, the cumulative fission yield of that specific fission product, and the total mass of actinides present in the sample. This method is sometimes referred to as the “Fission Product Monitor - Residual Heavy Atom” technique [35, 36] and calculates burnup in Fission per Initial heavy Metal Atoms (%FIMA). All fission yields were taken from ENDF/B-VII.1 [37]. A benefit of this burnup technique is that it requires no *a priori* knowledge of the sample. The burnup value and information about the fuel is used to calculate fission density. The fission density is the most consistent metric for comparing fuel performance across different experiments and will be used to compare performance metrics between the FUTURIX-FTA data, the AFC-1 data and other fast spectrum irradiations.

The ICP-MS results were able to produce isotope specific results for U-234, U-235, U-236, U-238, Pu-238, Pu-239, Pu-240, Pu-241, Pu-242, Np-237, Am-241, and Cm-244. The combined mass of Am-242 and Cm-242 was evaluated, as well as the combined mass of Am-243 and Cm-243. Higher mass minor actinides were not measured in detectable quantities. Fission product results were determined for all fission products from A=85 to A=146. Some masses were not determined due to interference from Zr in the fuels and double ionizations (around A=119).

There are six isotopes that work reliably for the ICP-MS technique in the FUTURIX-FTA fuel: La-139, Ce-140, Ce-142, Pr-141, Nd-145, and Nd-146. Burnup was determined from the average measured values of these fission products. The uncertainty of all mass spectrometry values is ±5% (2-sigma), and the derived burnup values are also considered no better than 5% relative uncertainty. The measured burnup values, the measured fission densities, and the calculated burnup for each rodlet are shown in Table 6. Both the low fertile rodlets (DOE1 and DOE3) match the calculations within the 5% relative uncertainty. There is more discrepancy in the non-fertile rodlets, likely attributable to the fact that the nuclear data used in the analyses are considerably less well known for Pu and Am as compared to that for U.

It is of interest to compare the isotopic mix of actinides at the end of the FUTURIX-FTA irradiation to that at the end of AFC-1 experiments. While this is expected to be sensitive to the differences in neutron spectra between the two testing environments, isotopic differences do not generally impact issues of fuel performance (i.e., materials behavior); however, fuel performance differences can be impacted by significant changes in chemical composition. Determining if the change in final minor actinide content impacts fuel performance could be important to informing future transmutation fuel tests in cadmium-

Table 6. Burnup values for FUTURIX-FTA and AFC-1 Sister Rodlets.

Rodlet	Simulation [26, 27, 13, 14] (%FIMA)	Measured Burnup (%FIMA)	Measured Fission Density (fissions/ cm^3)
Low-fertile Metallic (U-28.3Pu-3.8Am-2.1Np-31.7Zr)			
DOE1	9.1%	9.5%	2.08E+21
AFC-1H R1	18.0%	13.6%	2.94E+21
AFC-1H R4	26.7%	20.5%	4.82E+21
Non-fertile Metallic (Pu-10.5Am-0.3Np-41.6Zr)			
DOE2	15.5%	12.7%	2.01E+21
AFC-1D R1	15.7%	13.1%	1.79E+21
AFC-1D R4	22.6%	25.0%	3.57E+21
AFC-1G R1	14.1%	11.8%	1.70E+21
AFC-1G R4	20.3%	19.4%	2.77E+21
Low-fertile Nitride ($(U_{0.51}Pu_{0.27}Am_{0.14}Np_{0.08})N$)			
DOE3	1.6%	1.4%	4.50E+20
AFC-1Æ R6	2.9%**	1.8%	5.47E+20
AFC-1G R3	16.9%	10.4%	3.35E+21
Non-fertile Nitride ($(Pu_{0.85}Am_{0.15})N$+46.5ZrN)			
DOE4	4.1%	3.50%	4.08E+20
AFC-1Æ R1	4.0%**	1.7%	2.26E+20
AFC-1Æ R3	5.9%**	2.2%	2.86E+20
AFC-1Æ R4	6.4%**	2.7%	3.67E+20

* numbers preceding elements denote weight percent, subscript numbers represent mole percent. This is the as-fabricated composition not the nominal composition

** From EDF-8263 Draft document

filtered positions in ATR. A comparison between the FUTURIX-FTA and the AFC-1 rodlets is shown in Table 7 that displays the final actinide concentrations by mass for U-235 to Cm-244. A direct one-to-one comparison between these values cannot always be made because the uranium enrichment in each rodlet was varied to achieve the desired LHGR. The higher mass actinides are more comparable. The Pu enrichment was not varied so it is possible to compare Pu-239 content for samples of similar burnup. The Pu-239 content is in good agreement between FUTURIX-FTA and AFC-1 indicating the correct fission rate was established in the AFC-1 experiments as predicted by the analysis in Section 2. There is generally a higher concentration of Am-241 in the FUTURIX rodlets than in the AFC-1 rodlets, but there is much more Pu-241 (which decays to Am-241) in the AFC-1 rodlets. AFC-1G R3 is most notable for having 64 times more Pu-241 than DOE-3. AFC-1H R4 has 13 times more Pu-241 than DOE-1. This applies for mass 242, 243, and 244. The difference in Cm-244 between the FUTURIX-FTA rodlets is

Table 7. Actinide Composition of FUTURIX-FTA and AFC-1 Sister Rodlets

Rodlet	U-235	U-236	U-238	Np-237	Pu-238	Pu-239	Pu-240	Pu-241	Pu-242	Am-241	Am/ Cm-242	Am/ Cm-243	Cm-244
Low-fertile Metallic (U-28.3Pu-3.8Am-2.1Np-31.7Zr)													
DOE1	1.30E-03	3.86E-04	5.25E-01	2.52E-02	1.33E-02	2.95E-01	8.58E-02	3.93E-03	3.16E-03	4.41E-02	1.34E-03	3.34E-04	1.41E-05
AFC-1H R1	3.61E-01	3.40E-02	1.13E-01	2.33E-02	3.09E-02	2.93E-01	5.89E-02	3.38E-02	6.11E-03	3.41E-02	2.96E-03	2.39E-03	1.13E-03
AFC-1H R4	3.27E-01	5.07E-02	1.12E-01	2.26E-02	5.15E-02	2.76E-01	5.16E-02	5.30E-02	9.76E-03	3.03E-02	3.37E-03	4.55E-03	3.18E-03
Non-fertile Metallic (Pu-10.5Am-0.3Np-41.6Zr)													
DOE2	8.25E-04	6.35E-04	8.81E-04	7.18E-03	3.02E-02	5.81E-01	1.69E-01	7.06E-03	8.15E-03	1.88E-01	4.88E-03	7.80E-04	2.26E-05
AFC-1D R1	8.45E-04	5.22E-04	3.08E-03	4.70E-03	7.14E-02	5.66E-01	1.25E-01	5.84E-02	1.63E-02	1.30E-01	1.03E-02	7.18E-03	2.74E-03
AFC-1D R4	9.23E-04	5.56E-04	3.59E-03	4.15E-03	1.06E-01	5.09E-01	1.34E-01	8.08E-02	2.62E-02	1.02E-01	8.25E-03	1.25E-02	7.08E-03
AFC-1G R1	6.46E-04	4.19E-04	2.36E-03	1.19E-01	5.81E-02	6.05E-01	1.28E-01	5.79E-02	5.50E-03	1.69E-02	4.76E-04	2.28E-03	1.10E-03
AFC-1G R4	7.81E-04	4.61E-04	1.65E-03	9.45E-02	7.74E-02	5.67E-01	1.29E-01	8.48E-02	9.15E-03	2.41E-02	6.96E-04	4.22E-03	2.77E-03
Low-fertile Nitride (($U_{0.51}Pu_{0.27}Am_{0.14}Np_{0.08}$)N)													
DOE3	1.64E-03	8.93E-05	5.26E-01	8.77E-02	7.94E-03	2.30E-01	1.79E-02	3.06E-04	8.93E-04	1.26E-01	8.47E-04	1.19E-04	2.31E-06
AFC-1Æ R6	2.22E-01	3.73E-03	2.72E-01	9.81E-02	1.25E-02	2.45E-01	1.80E-02	3.56E-03	1.61E-03	1.22E-01			
AFC-1G R3	1.64E-01	2.22E-02	2.92E-01	5.80E-02	9.92E-02	2.28E-01	2.37E-02	1.96E-02	1.02E-02	6.74E-02	6.14E-03	4.05E-03	1.62E-03
Non-fertile Nitride (($Pu_{0.85}Am_{0.15}$)N+46.5ZrN)													
DOE4	3.33E-03	1.50E-04	2.04E-02	2.88E-02	8.57E-03	6.80E-01	5.62E-02	7.82E-04	1.36E-03	1.99E-01	1.31E-03	5.94E-05	2.69E-07
AFC-1Æ R1	0.00E+00	0.00E+00	0.00E+00	2.16E-02	1.94E-02	5.17E-01	3.69E-02	6.66E-03	4.26E-03	3.94E-01			
AFC-1Æ R3	0.00E+00	0.00E+00	0.00E+00	2.10E-02	3.49E-02	5.00E-01	3.75E-02	9.59E-03	6.92E-03	3.90E-01			
AFC-1Æ R4	6.93E-04	4.80E-05	2.34E-03	2.29E-02	3.51E-02	5.28E-01	4.17E-02	1.05E-02	6.72E-03	3.51E-01			

* numbers preceding elements denote weight percent, subscript numbers represent mole percent. This is the as-fabricated composition not the nominal composition

quite striking with AFC-1G R3 having 700 times more Cm-244 than DOE-3, AFC-1D R4 has 313 times more than DOE-2 and AFC-1H R4 has 224 times more Cm-244 than DOE-1. This is not unexpected, as the cadmium-filtered positions used in ATR have a neutron spectrum that results in a higher capture-to fission-ratio for all actinides (and other nuclides *e.g.,* fission and activation products) than does a genuine fast neutron spectrum. These results also demonstrate that while testing in cadmium-filtered positions in ATR may be able to approximate fuel performance (i.e., material behaviors) expected under fast reactor conditions, it will not be able to approximate the isotopic transmutation behaviors experienced by fuels in fast reactors.

3.1.6 Metallography

For both FUTURIX-FTA and AFC-1 samples, optical microscopy was performed on fuel cross sections to investigate irradiation induced features in the fuel microstructure. Neutron radiography and the visual exams were used to guide the sectioning of the fuel at the approximate mid-plane of the fuel column. The sectioned fuel was placed in a met mount and back filled with epoxy. The FUTURIX-FTA mounts had epoxy that contained approximately 15 wt. % graphite for conductivity to facilitate subsequent examination using electron microscopy. After polishing, samples were transferred to the HFEF Met Box for examination on a Leitz MM5RT metallograph. The previously prepared samples from AFC-1D, AFC-1G, and AFC-1H were re-polished and reexamined in the summer of 2016. Sample preparation techniques and experience improved from the initial examination of this fuel prompting such a reanalysis. It was, however, not possible to reexamine the lower burnup AFC-1Æ samples. Microscopy from these samples is reproduced from Reference 13.

The cross section for DOE1 MNT-20Y (U-29Pu-4Am-2Np-30Zr) was prepared twice. The surface revealed by the initial preparation is seen in Figure 39, and in greater detail in Figure 41, and the surface revealed by the second preparation is seen in Figure 40, and in greater detail in Figure 42. The first preparation revealed a surface where the central region was highly porous. It was assumed that some of the highly porous fuel structure had fallen out during sample preparation resulting in the large black void seen in Figure 39. This void was actually visible through the hot-cell window. With the amount of central porosity seen in Figure 39 and Figure 41, the Cs behavior indicated from Figure 35 appears more reasonable. An alternative explanation to the difference in microstructure between the two cross sections is that the void observed in Figure 39 is that an actual pressurized void had formed and all the porosity locally migrated to the center, leaving the fuel in the outer radii denser. In contrast, the local porosity in Figure 40 is more evenly distributed. In both preparations the porosity is spherical in shape throughout most of the fuel. In the second preparation, the porosity is smaller and somewhat lenticular in the outer periphery of the fuel. This would tend to indicate that the underlying crystal structure of the fuel material is cubic everywhere except the outer 500 µm. The U-Pu-Zr ternary phase diagram [38] suggests that any of the DOE1 or AFC-1H R1, R4 fuel operating above 600°C should be a cubic (bcc) phase. This phase is γ-(U, Zr) and ε-Pu. However, with the amount of porosity present, the typical porosity behavior of binary and ternary U-Zr and U-Pu-Zr alloys may not hold. In historic binary or ternary metallic fuels, lenticular pores can be formed at temperatures below the γ phase transition temperature (776°C) [38]. The cladding temperature of DOE1 was calculated to be approximately 550°C, so there should be a region of the fuel showing non-spherical porosity that was irradiated below the γ-U phase transition temperature [26]. There is also a small (~20 µm) interaction layer at many locations between the fuel and the cladding. Optically, this cannot be positively identified. This may be the initiation of a FCCI layer, or it may be an artifact of fabrication. There is also a Zr rich layer at the outer edge of the as-fabricated samples [24].

Optical microscopy for AFC-1H R1 and AFC-1H R4 are shown in Figure 43, Figure 44, Figure 45, and Figure 46. The temperature difference between R1 (peak cladding temperature ~ 400°C) and R4 (peak cladding temperature ~ 495°C) is readily apparent. The pore structure displayed by AFC-1H R1 is very similar to that seen in the periphery of both FUTURIX-FTA DOE1 and AFC-1H R4. The radial pore distribution of AFC-1H R4 appears to be similar to the distribution in FUTURIX-FTA DOE1. It is likely that Zr redistribution occurred in AFC-1H R4, while it seems unlikely in AFC-1H R1. The crystal structure arguments made in the previous paragraph apply to AFC-1H R4. Additional electron microscopy and or EPMA analysis will be required to confirm if the elemental distributions in FUTURIX-FTA and AFC-1H are similar.

The cross section from DOE2 MNT-21Y (Pu-12Am-40Zr) is shown in increasing detail in Figure 47, Figure 48, and Figure 49. The cladding has several spots with debris and tarnishing artifacts resulting from polishing. The black marks on the cladding in Figure 47 should not be mistaken for cladding degradation. This cross section shows evidence of constituent redistribution and phase separation. There are several rings of microstructure present in Figure 47 that suggest different phases that were present during irradiation, and these phases are likely driven by different the thermal gradient (spanning a miscibility gap in the phase equilibria) present in the fuel during irradiation. The Pu-Am-Zr system is not as well understood as the U-Zr or the U-Pu-Zr system, but many of the same observations made on the DOE1 cross section can be made and tied back to known properties of the Pu-Zr system. X-ray diffraction (XRD) performed on an as-fabricated fuel specimen revealed the predominant microstructure to be δ-(Pu,Zr) [24]. During irradiation the cladding temperature was ~ 550°C, so it is likely that during irradiation both δ-(Pu,Zr) and ε-(Pu,Zr) were present in the fuel. Both of these phases are cubic, and the morphology of the porosity present in the irradiated fuel also suggests a cubic crystal structure. As in DOE1, there is a ~ 20μm layer that is likely a Zr rich layer formed at fabrication. There are at least 5 distinct microstructural zones apparent in the fuel. The general boundary for these zone are shown in Figure 47 and are labeled A to E going from the center to the outer radius. The first three zones (C, D, E) from the outer radius of the fuel inward about 1 mm all have low levels of porosity and varying amounts of what appears to be phase separation (suggested by the different colors in microscopy, which can often indicate various different levels of oxidation). Certain local compositions and microstructures oxidize faster than others, presenting different colors. In the next 750 μm (zone B), the porosity of the fuel changes significantly and becomes much larger. The color of the fuel matrix also suggests that this is a more homogeneous phase in the fuel. This is all visible in Figure 47 and Figure 48 as well. The interior of the fuel (zone A) has a great deal of phase separation. In Figure 48, one of the phases is much more susceptible to tarnish and appears orange in the collected microscopy. The orange phase tends to cluster and is surrounded by a lighter matrix phase. The matrix phase is shown in detail in Figure 49. If it is assumed that the appearance of the stacked structure is indication of a different chemical phase, rather than a different crystallographic orientation in the material, the matrix phase has a stacked structure that is suggestive of the decomposition of γ(U,Zr) into αU and δUZr_2. The stacked structure in this fuel could be the decomposition of ε-(Pu,Zr) into δ-(Pu,Zr) and αZr. If Zr redistribution did drive additional Zr up the temperature gradient to the center of the fuel, this explanation is also more likely. The exact nature of these phases and the location of the Am in the fuel will require further investigation, likely requiring examination by the EPMA. Micro-XRD and the preparation of transmission (TEM) lamella using a Focused Ion Beam (FIB) could also be helpful to better understand this system.

Optical microscopy from AFC-1D R1, AFC-1D R4, AFC-1G R1 and AFC-1G R4 are shown in Figure 50, Figure 51, Figure 52, Figure 53, Figure 54, Figure 55, Figure 56, and Figure 57. Both AFC-1D R1 and AFC-1G R1 were operated at lower temperatures than the R4 rodlets. The porosity in the AFC-1D rodlets appears different from the porosity seen in FUTURIX-FTA DOE2. Based on the neutron radiography of AFC-1D R1, the cross section taken for metallography happened to be taken from an area with a large amount of porosity. Examination of another sample from this rodlet is warranted to determine whether other axial locations exhibit similar microstructures. It is not clear why the porosity at the periphery of AFC-1D R1 is so large, but this is a departure from the DOE2 microstructure and historical metallic fuel behavior. The AFC-1G R1 and R4 microstructures are closer to the FUTURIX-FTA microstructure. The AFC-1G R1 microstructure may have been smeared during sample preparation in the central area of the fuel. Historical experience would suggest that there should be more porosity in this region. The AFC-1G R4 microstructure is the closest to FUTURIX-FTA DOE2. In this fuel rodlet the crystal structure arguments from the previous paragraph also hold. However, the higher magnification data was not collected, so it is not known if the stacked structure seen in FUTURIX-FTA DOE2 is also present in AFC-1G R4. As with the low-fertile metallic alloy, SEM, EPMA, TEM, and other advanced characterization techniques would be helpful to better understand this system.

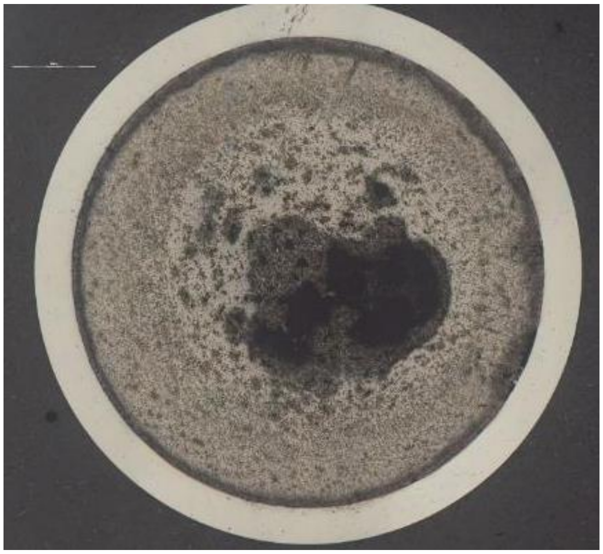

Figure 39. Montage of images collected from first preparation of cross section of DOE1 (low-fertile metallic).

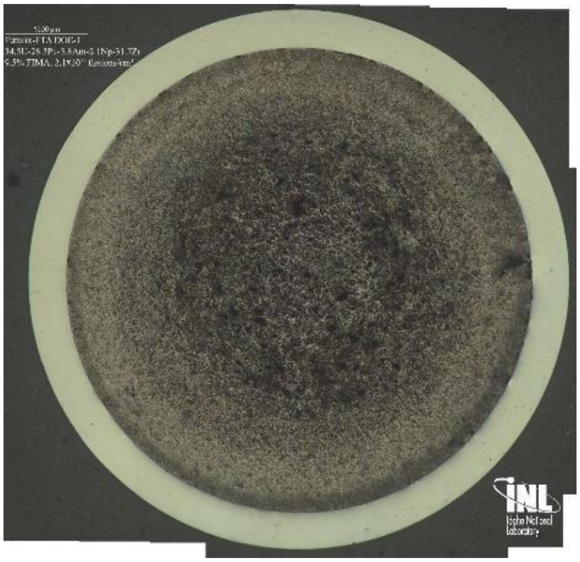

Figure 40. Montage of images collected from second preparation of cross section of DOE1 (low-fertile metallic).

Figure 41. Higher magnification detail of radial microstructure revealed in first preparation of DOE1 (low-fertile metallic).

Figure 42. Higher magnification detail of radial microstructure revealed in second preparation of DOE1 (low-fertile metallic).

Figure 43. AFC-1H R1 cross section (low-fertile metallic).

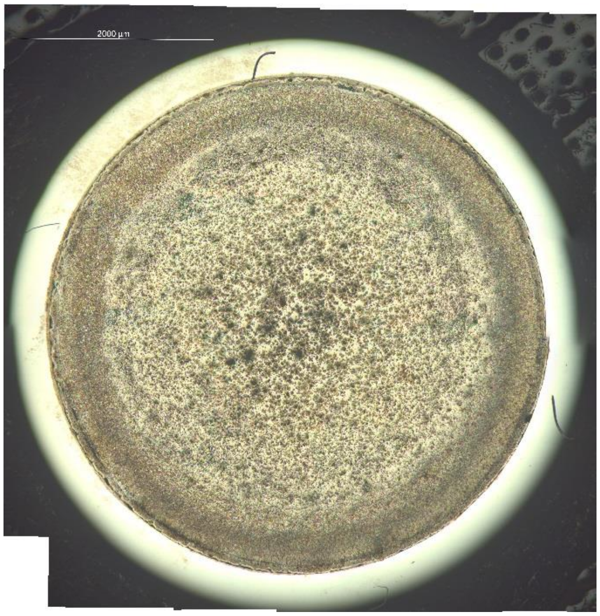

Figure 44. AFC-1H R4 cross section (low-fertile metallic).

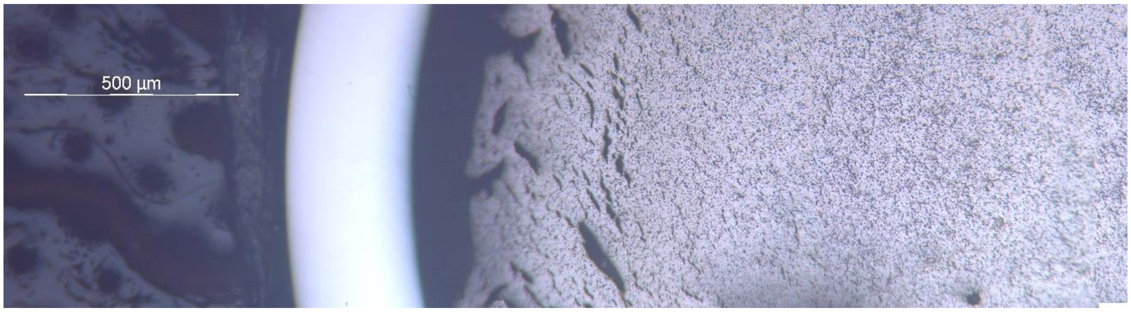

Figure 45. Higher magnification detail of radial microstructure revealed in AFC-1H R1 (low-fertile metallic).

Figure 46. Higher magnification detail of radial microstructure revealed in AFC-1H R4 (low-fertile metallic).

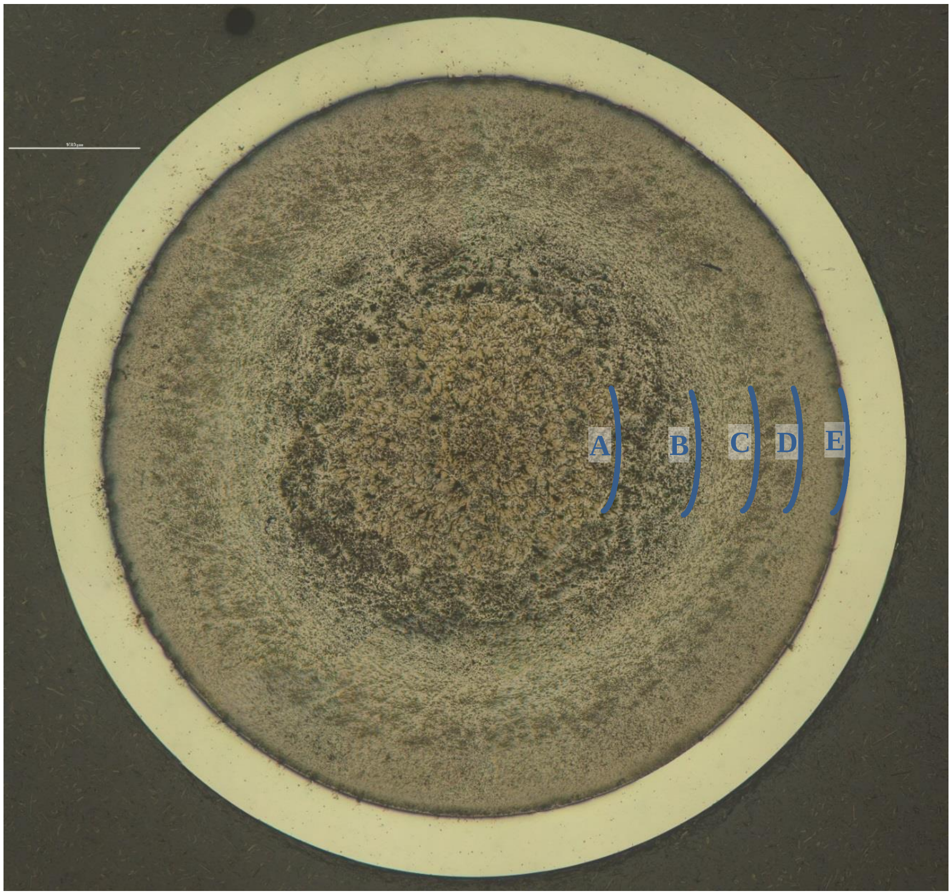

Figure 47. Montage of images collected from cross section of DOE2 (non-fertile metallic) with labels that delineate the different microstructural zones.

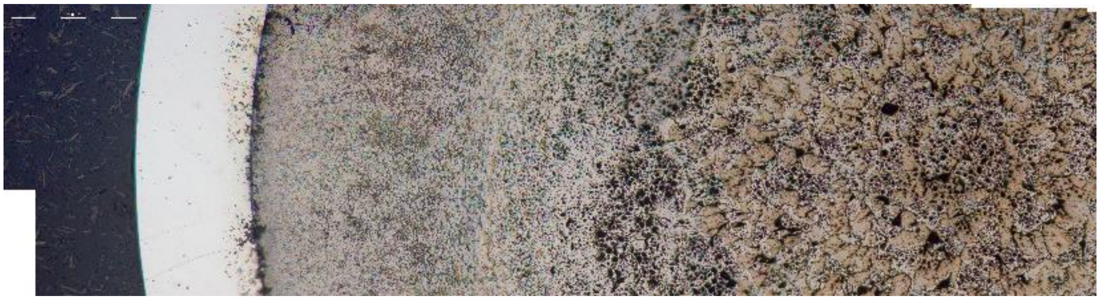

Figure 48. Higher magnification detail of radial microstructure revealed in DOE2 (non-fertile metallic).

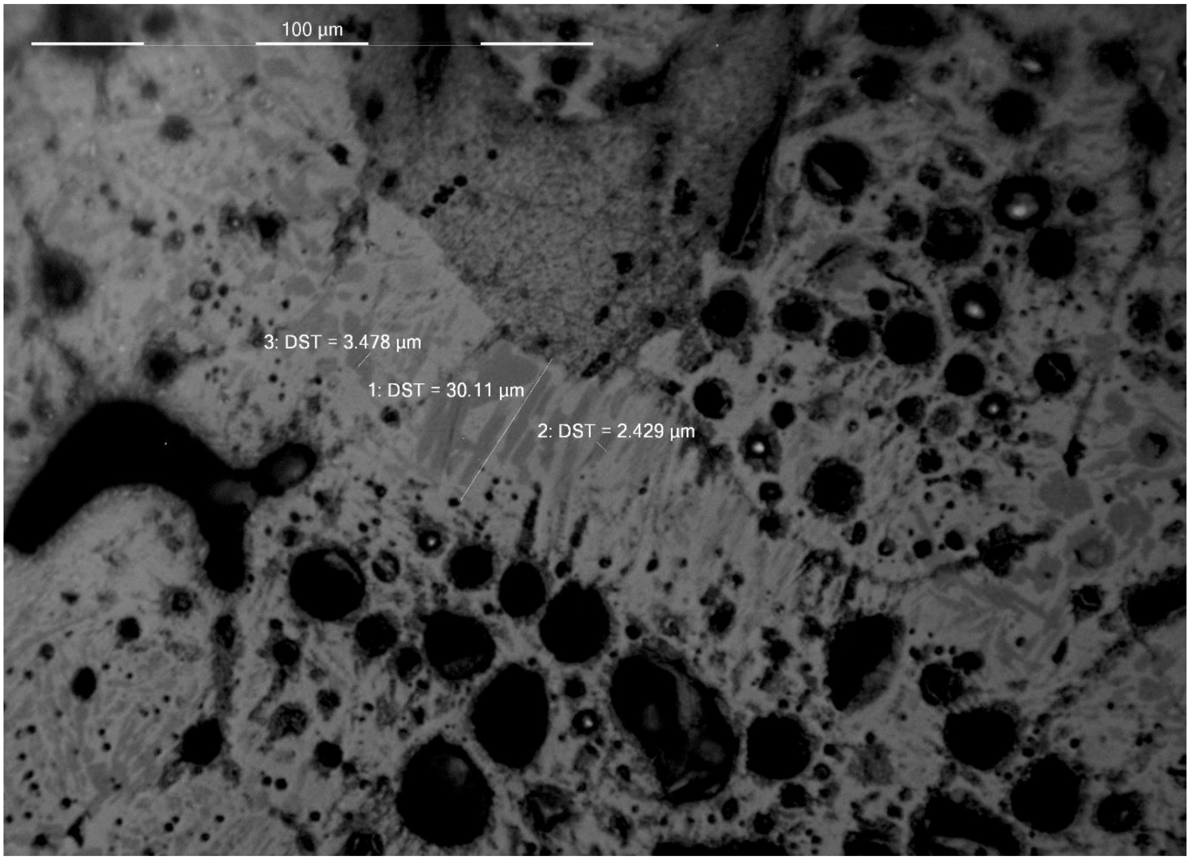

Figure 49. Detail of phase separation present in the central region of DOE2 MNT-21Y (non-fertile metallic).

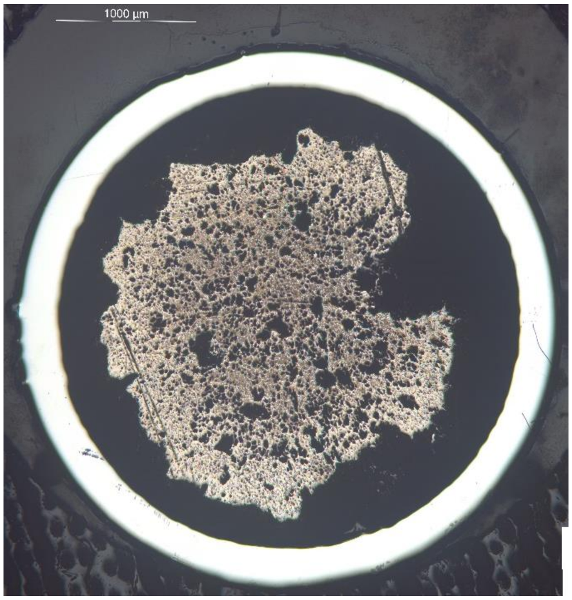

Figure 50. AFC-1D R1 cross section (non-fertile metallic).

Figure 51. AFC-1D R4 cross section (non-fertile metallic).

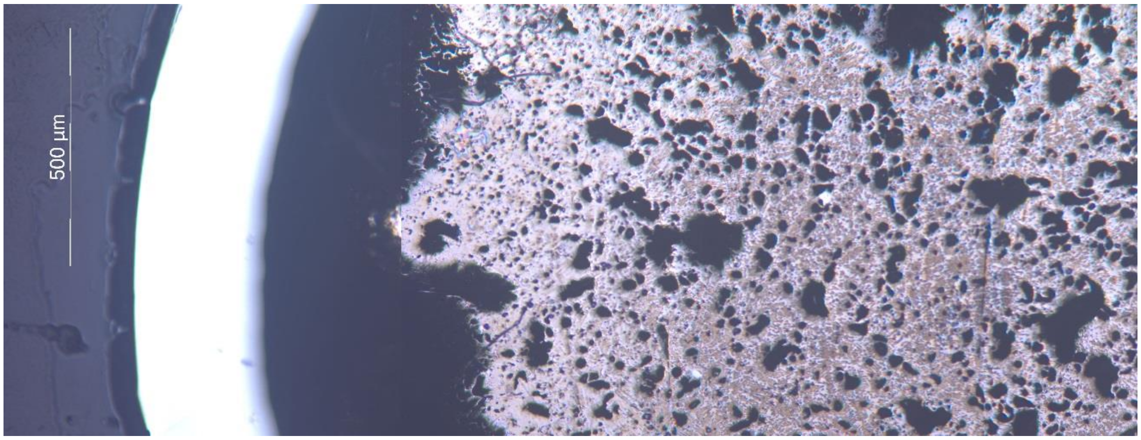

Figure 52. Higher magnification detail of radial microstructure revealed in AFC-1D R1 (non-fertile metallic).

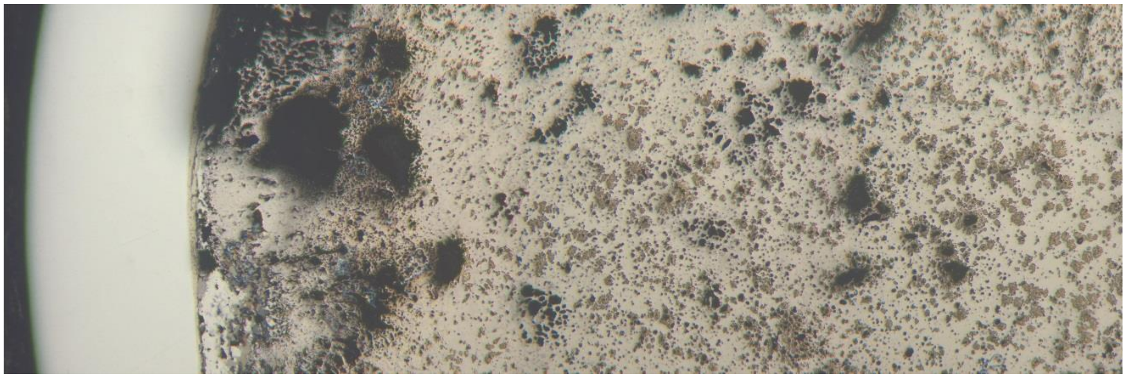

Figure 53. Higher magnification detail of radial microstructure revealed in AFC-1D R4.

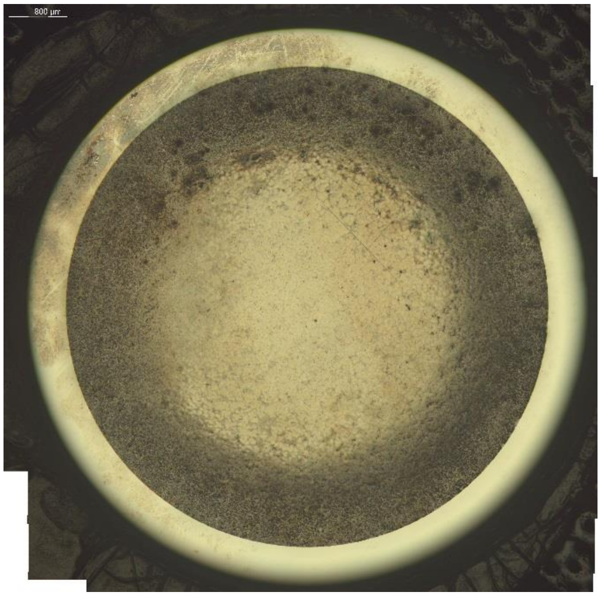

Figure 54. AFC-1G R1 cross section (non-fertile metallic).

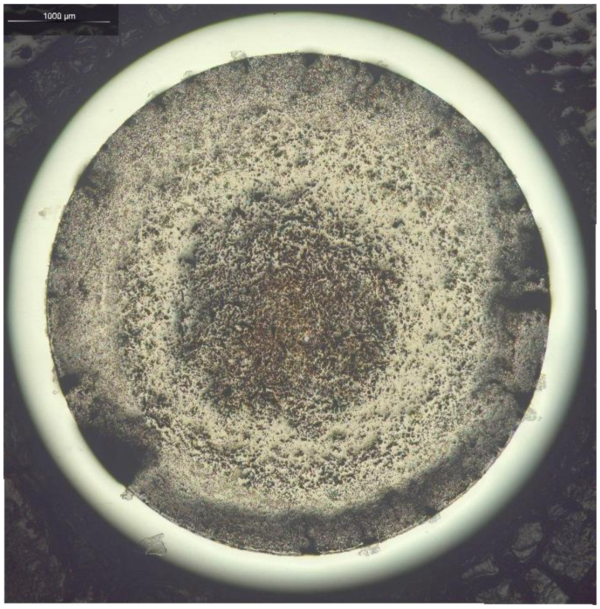

Figure 55. AFC-1G R4 cross section (non-fertile metallic).

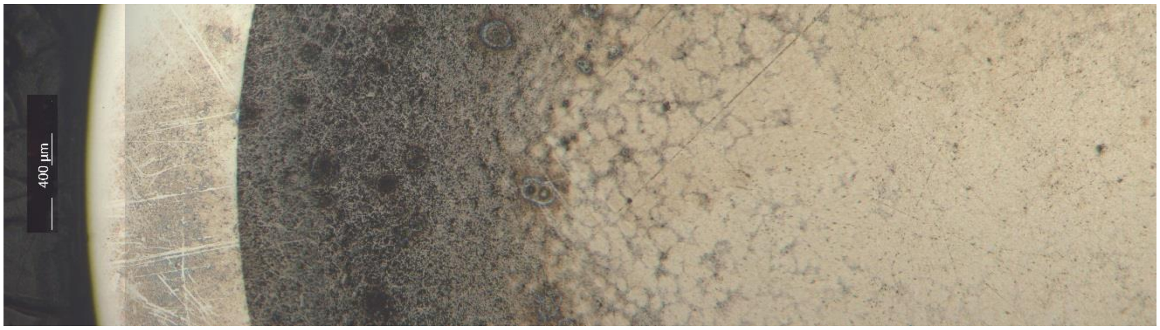

Figure 56. Higher magnification detail of radial microstructure revealed in AFC-1G R1 (non-fertile metallic).

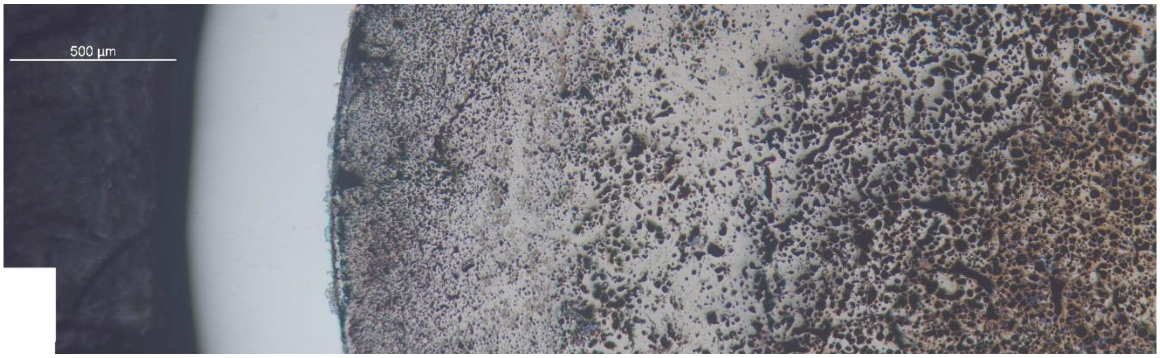

Figure 57. Higher magnification detail of radial microstructure revealed in AFC-1G R4 (non-fertile metallic).

The nitride fuels are more straight forward than the metallic fuels largely due to their lower burnup. Optical microscopy images from the prepared cross section from DOE3 (($U_{0.50}Pu_{0.25}Am_{0.15}Np_{0.10}$)N) are shown in Figure 58 and Figure 59. The microstructure in Figure 58 and Figure 59 is largely unchanged from the as-fabricated microstructure [25]. This is demonstrated in Figure 60. A similar comparison is shown in Figure 61 for the cross section prepared from DOE4. A higher magnification image of DOE4 is shown in Figure 62. Again, this pellet has not changed much from the as-fabricated microstructure. As with the as-fabricated pellets, there is a lighter lower porosity rind on the pellet and a higher porosity center. There are also several areas of large grains interspersed with smaller grained material. There is not consistent evidence of any fission product phases forming in this fuel which is likely due to the relatively low burnup of this fuel sample. With nitride fuel, as with oxide fuel, it is possible to create an Ellingham diagram to look at the thermodynamic stability of the fission product nitrides versus the stability of the constituent actinide nitrides. If a higher burnup had been achieved it would have been reasonable to expect noble metal precipitates (Mo, Tc) analogous to what is seen in oxide fuels. Other noble metals (Pd, Ru, Rh) may form intermetallics with the actinides which might be detrimental to long term fuel performance through the creation of low melting phases. At the cladding temperature of 550°C, some rare earths (Pr, Nd, Sm, Ce) will form stable nitrides, while others (La, Eu) will not, which might cause longer term problems with FCCI. The most thermodynamically stable nitride fission product is ZrN which is also used to stabilize the non-fertile nitride pellets.

The optical microscopy for the AFC-1Æ nitride compositions is shown in Figure 63, Figure 64, Figure 65, and Figure 66. The microstructure observed in the AFC-1 Æ nitrides is similar to what was seen in FUTURIX-FTA and similar to the as-fabricated microstructure. There is more cracking in the AFC-1Æ cross sections than in the FUTURIX data. This may be due to different irradiation conditions, but the cracking is likely due to handling or storage damage, sample preparation, or fabrication defects.

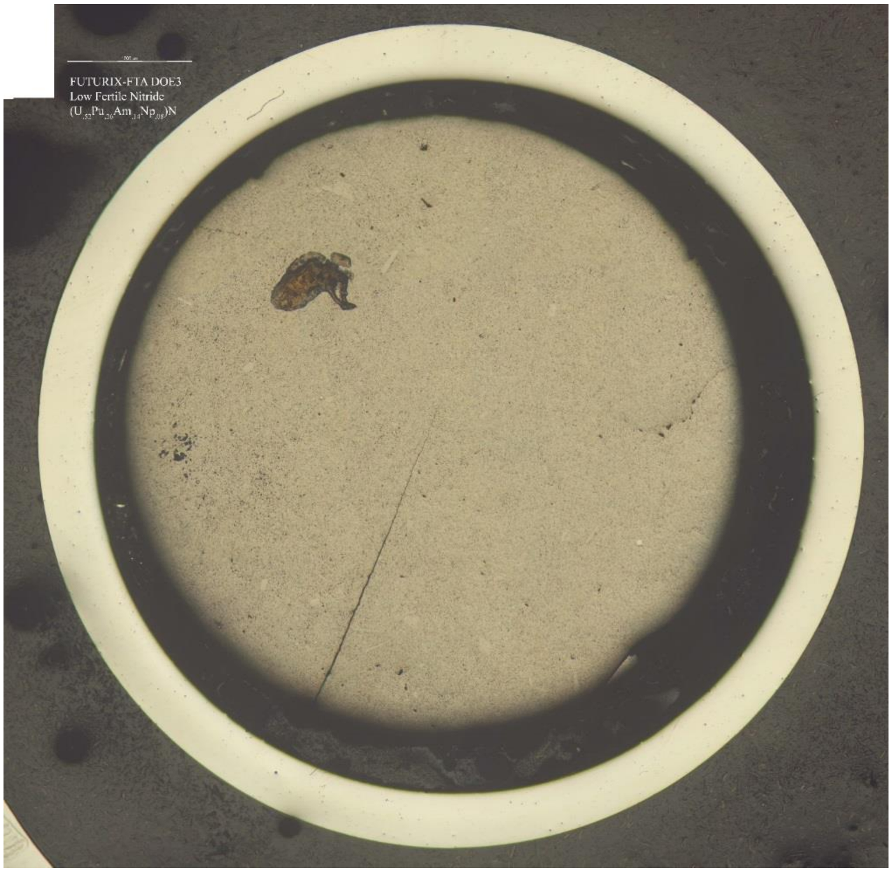

Figure 58. Montage of images collected from cross section of DOE3 (low-fertile nitride). (There is a large smudge on upper left of the DOE3 cross section that is an artifact from preparation and could not be removed with wiping.)

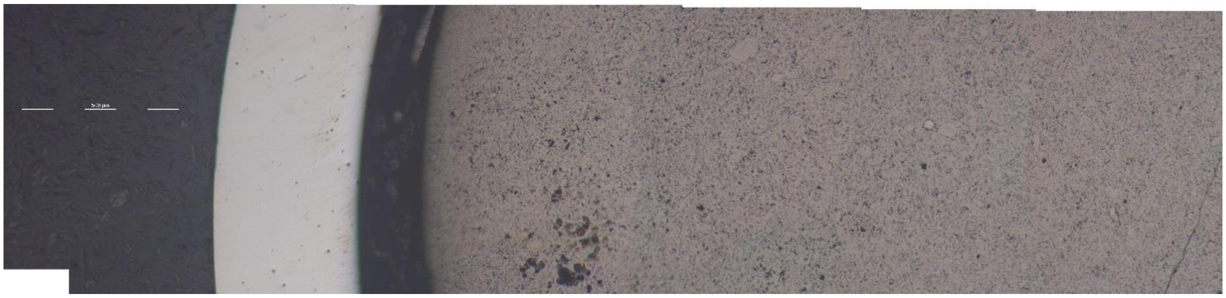

Figure 59. Higher magnification detail of radial microstructure revealed in DOE3 (low-fertile nitride).

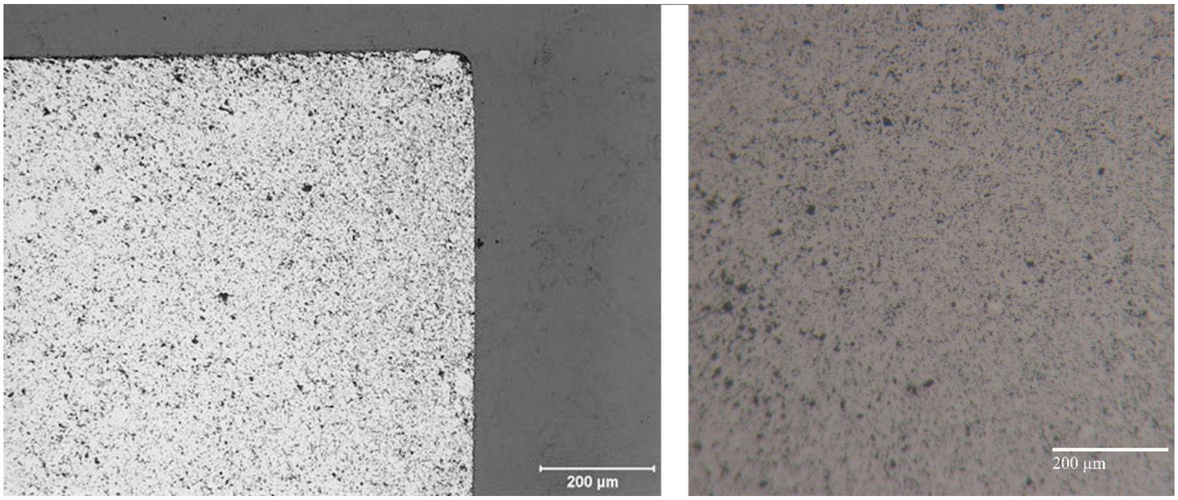

Figure 60. DOE 3 (low-fertile nitride) As-fabricated (left) microstructure compared to irradiated microstructure (right).

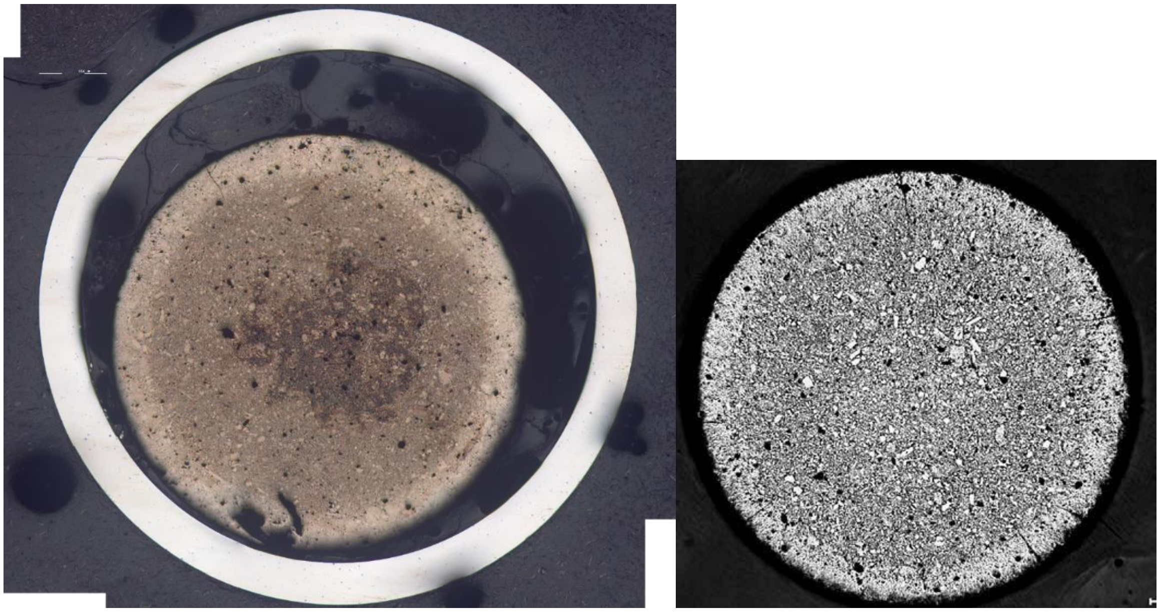

Figure 61. Montage of images collected from cross section of DOE4 (non-fertile nitride) (left) compared to the as-fabricated pellet microstructure (right).

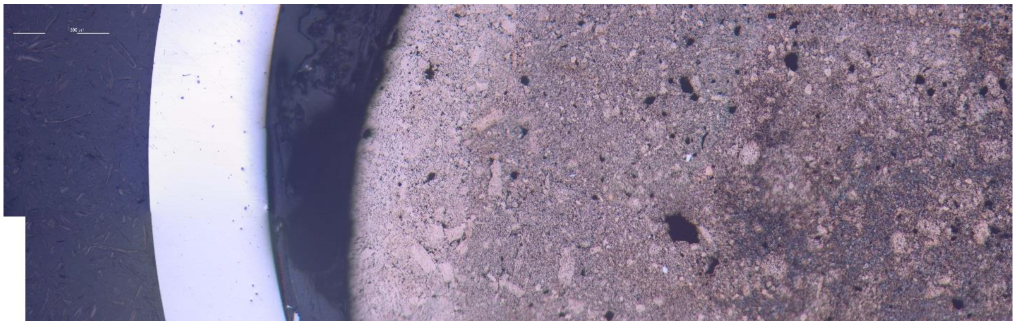

Figure 62. Higher magnification detail of radial microstructure revealed in DOE4 (non-fertile nitride).

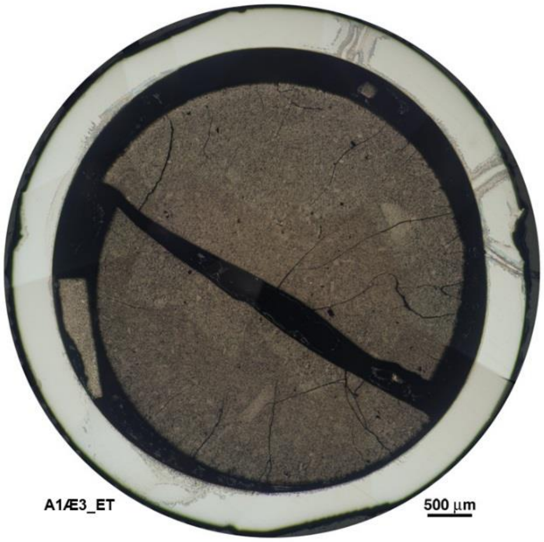

Figure 63. AFC-1Æ R1 cross section (non-fertile nitride).

Figure 64. AFC-1 Æ R3 cross section (non-fertile nitride).

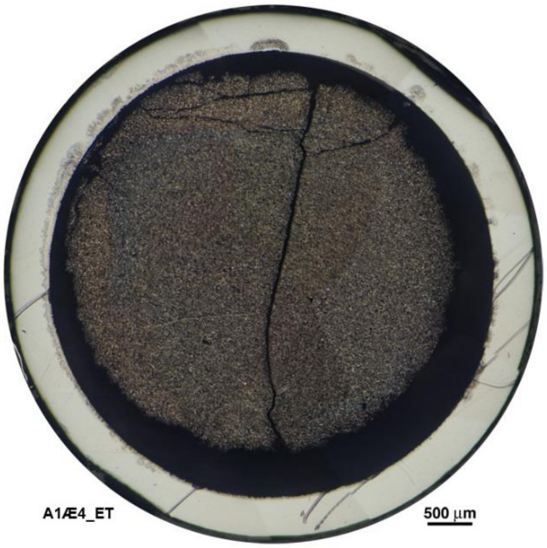

Figure 65. AFC-1 Æ R4 cross section (non-fertile nitride).

Figure 66. AFC-1 Æ R6 cross section (non-fertile nitride).

3.1.7 Electron Microscopy

Only a limited amount of electron microscopy has been performed on irradiated transmutation fuels. The dose rates from full cross sections of irradiated fuels are typically too high for hands-on handling and loading into electron microscopes that are typically operated in unshielded radiological facilities. The dose rates often cause issues with the electronics in electron microscopes and their associated detectors. In spite of these challenges, some work has recently been attempted. Additional samples are expected to be examined in the future as possible.

Recently, it was possible to place a FUTURIX-FTA DOE1 sample shown in Figure 40 in the SEM at the INL Electron Microscopy Laboratory (EML). The data obtained is still being analyzed, but some highlights are included here. A montage of back-scattered electron (BSE) imaging is shown in Figure 67. In the upper right hand area of this image is some copper tape used to ground the sample electrically. In this figure, brighter areas indicate areas of higher electron density associated with higher atomic number elements. The same pore size distribution seen in the optical microscopy is also seen in the electron microscopy. The redistribution of Zr is less readily apparent than what has historically been seen in U-10Zr [16] or U-20Pu-10Zr [39], although Zr redistribution is expected to be highly composition dependent. At magnifications higher than that used for Figure 67, it is possible to observe some Zr redistribution where the Zr concentration is higher in the center of the fuel. Elsewhere in the fuel there are two observed phases throughout the fuel. One phase is a higher Zr phase that is approximately 35% U, 30% Pu, and 25% Zr. The other phase is a lower Zr, higher U phase that is approximately 60%U, 30% Pu and 10% Zr. In the mid-radius, these phases are larger (10-30µm) than the outer radius where the phases are finer (1-15µm). A higher magnification BSE image is shown in Figure 68 that details the near cladding microstructure observed throughout the fuel. Several features are indicated in Figure 68 as key features. The cladding is AIM1, which contains ~ 0.5 wt.% Ti. It appears the Ti has precipitated in the cladding during irradiation. Next to the cladding is a layer of U, Pu, Zr, Si, and possibly some Am. This layer of Si is an artifact from fabrication where Si from the quartz mold enters the fuel and was observed after fabrication [24]. The Zr layer is also an artifact from fabrication where Zr from the wash used on the quartz enters the fuel and was observed in fabrication also [24]. There are precipitates of Lanthanides (La, Ce, Nd, and others) near the Zr layer. However there does not appear to be any attack of the cladding from the major fission product lanthanides (La, Ce, Nd). The higher Zr phase and the lower Zr phase mentioned previously are also indicated. The most significant feature observed in Figure 68 is an infiltration of Am and Sm into the cladding. Both of these elements have high vapor pressures. It is suspected that this infiltration is assisted by these high vapor pressures, but more research into the phenomenon is needed.

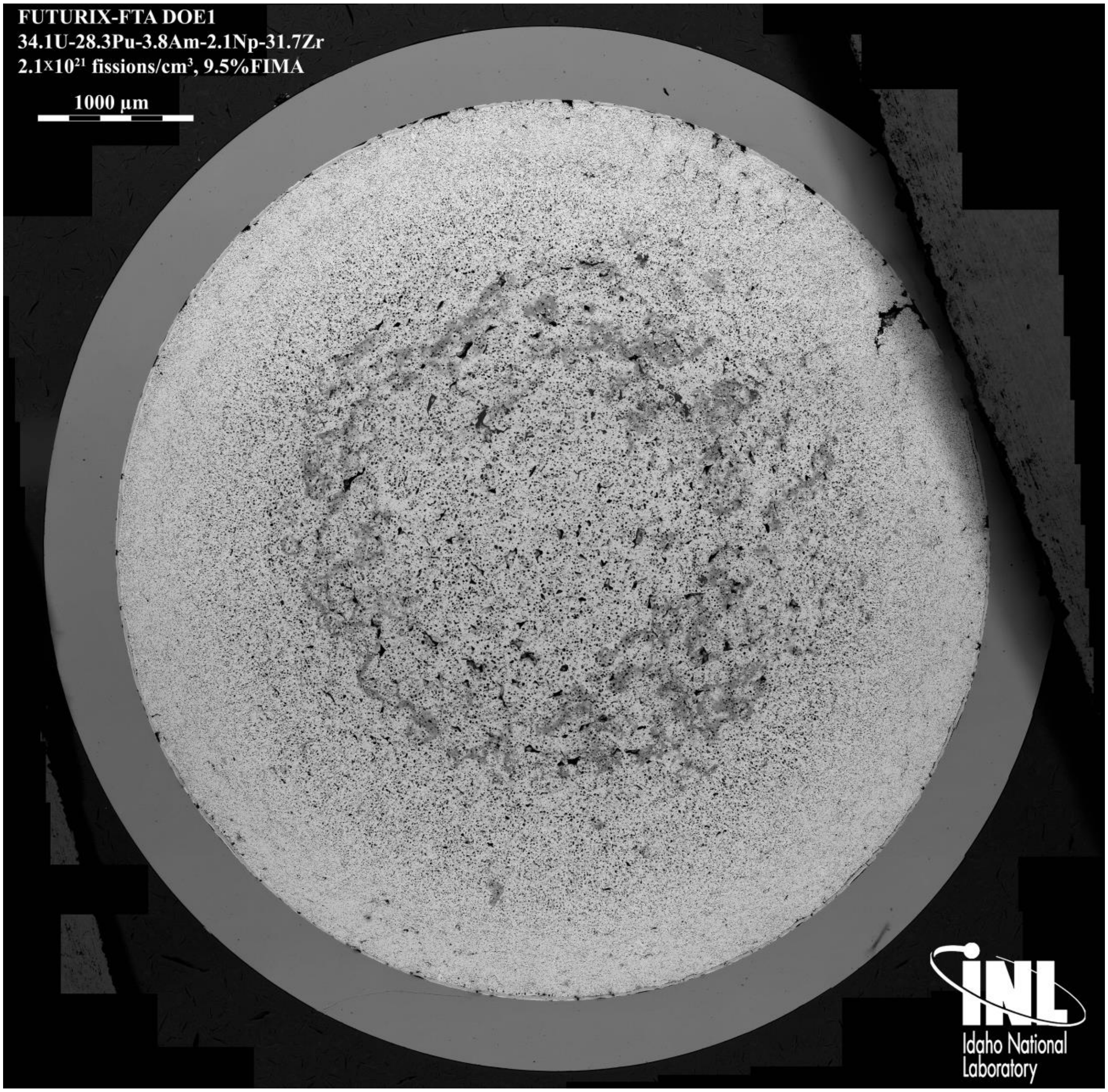

Figure 67. Back-scatter electron imaging of FUTURIX-FTA DOE1 (U-29Pu-4Am-2Np-30Zr) (low-fertile metallic).

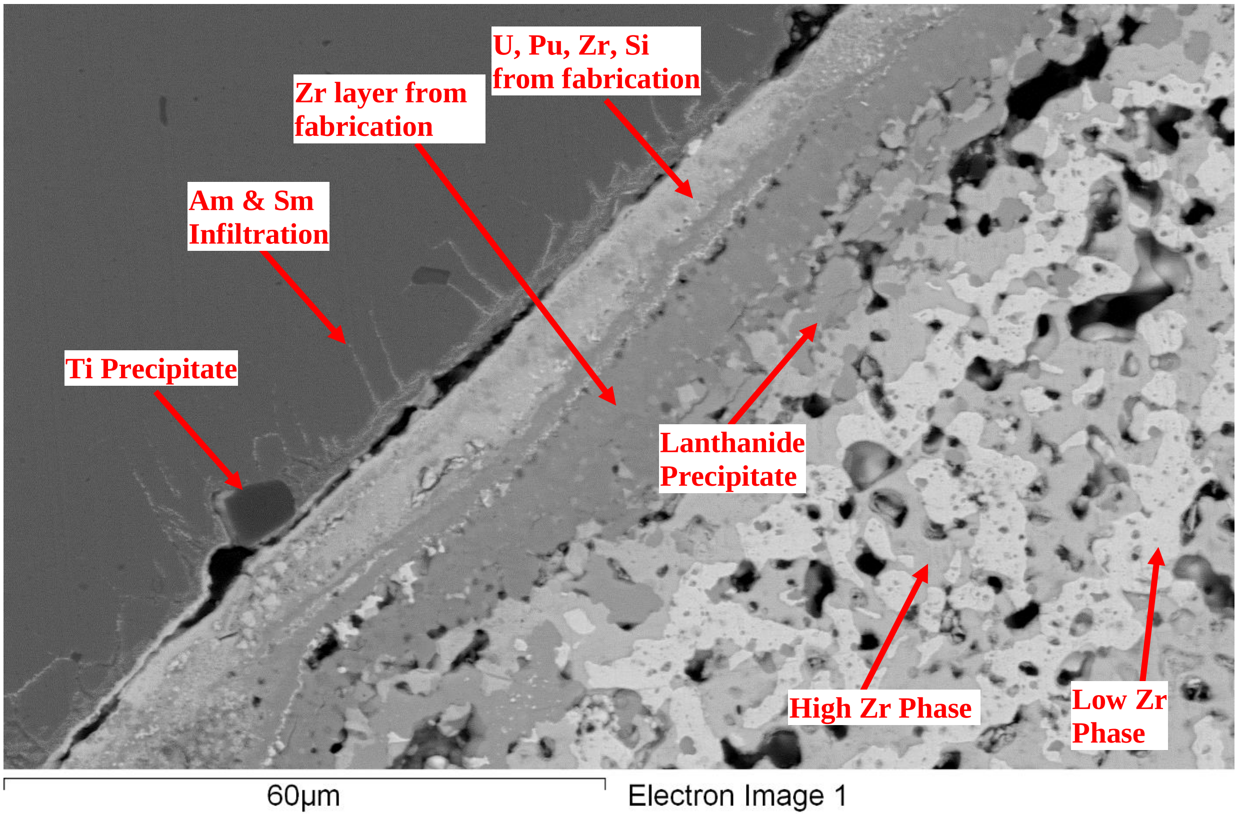

Figure 68. High magnification BSE detail of the DOE1 (low-fertile metallic) microstructure near the cladding.

3.1.8 EPMA

Currently, EPMA examination of the prepared cross section from FUTURIX DOE1 (low-fertile metallic) is planned to begin August 2017. As this data is collected, it will be added to subsequent versions of the Spectrum Comparison Report.

3.2 MOX Section

3.2.1 AFC-2C/D vs Literature

AFC-2C and AFC-2D were irradiations of MOX fuels with minor actinide additions and significant variations in oxygen-to-metal ratios performed in Cd-filtered positions in the ATR. There have been no experiments performed in a fast reactor on identical compositions, so no direct comparisons are possible. In future revisions of this report, comparisons to similar MOX fuels will be considered as appropriate.

3.2.2 Supporting Analyses

To be added at a later date.

4. FUTURE COMPARISONS

Comparisons between other cadmium-filtered ATR irradiation tests and historic irradiations in fast reactors are planned for the future. As the data for these comparisons is collected, they will be incorporated into future revisions of this report.

4.1 AFC-3F vs. EBR-II/FFTF Legacy (MFF, IFR-1)

The AFC-3F irradiation experiment is a cadmium-filtered test in ATR that has been designed to compare the fuel performance of U-10Zr and U-20Pu-10Zr metallic fuels that are fabricated using counter gravity injection casting versus arc-melting with drop casting. When PIE data from AFC-3F becomes available (~2020), the performance of these legacy metallic fuel alloys irradiated in ATR will be compared to U-10Zr and U-20Pu-10Zr fuels irradiated in EBR-II and the Fast Flux Test Facility (FFTF) and incorporated into a future revision of the Spectrum Comparison Report.

4.2 X-501 (G591)

The X-501 experiment that was conducted late during the operation of EBR-II was meant to evaluate the irradiation behavior of U-20Pu-10Zr fuel with minor additions of Am and Np. Two sister pins (Elements G582 and G591) were fabricated by counter-gravity injection casting [40] and were irradiated in EBR-II to a peak burnup of 7.6 at.% HM [41]. Only limited PIE was performed on G582. A more systematic PIE effort on G591 has been planned and is in progress at HFEF. When available, results from the comparison of these data with data from the AFC-1 series of irradiations in ATR will be incorporated into a future revision of the Spectrum Comparison Report.

5. CONCLUSIONS

The objective of cadmium-filtered testing in the ATR has been to create a temperature profile inside of test fuel rodlets that is nearly prototypic of corresponding fast reactor conditions. It is conceded that not all conditions within this testing environment are fully prototypic of a fast reactor (e.g., the fast flux does not reach levels expected in a fast reactor, and the thermal flux is not entirely eliminated). This report presents analyses that show that such a nearly prototypic temperature profile is achieved in test fuel rodlets irradiated in cadmium-filtered positions in ATR, which should allow for the study of fuel performance phenomena that are primarily dependent upon the conditions of temperature and temperature gradient inside the fuel. Validation of this assertion has been undertaken by comparing fuel performance phenomena observed in fuels irradiated in cadmium-filtered positions in ATR to similar or identical fuels irradiated under similar conditions in genuine fast reactors.

This report documents a preliminary comparison of fuel performance data available from the testing metallic, oxide, and nitride fuels in cadmium-filtered positions in the ATR to the performance of identical or similar fuels irradiated in genuine fast reactors. Although a variety of fuel performance metrics are presented, particular attention is paid to those phenomena that are primarily, or significantly, dependent on conditions of temperature and temperature gradient with the fuel. Comparisons showed how formation of a columnar grain region in oxide fuels is impacted by the radial power distribution in the fuel. In an unfiltered ATR neutron spectrum, significant power is shifted to the fuel pellet periphery, requiring a much higher LHGR to achieve formation of the columnar grain region. Use of cadmium-filtering results in removal of the vast majority of thermal neutrons seen by the experimental test fuels, which tends to flatten the radial power distribution similar to the essentially flat radial power distribution that would exist in a fast reactor. This effect was demonstrated by modeling formation of the columnar grain region in both cadmium-filtered ATR and typical SFR neutron spectra, which confirmed the similarity of oxide fuel behavior in these two conditions. Recognizing that modeling of columnar grain region formation is an established practice to validate temperature analyses of fast reactor oxide fuel, these results provide a sound foundation for establishing the relevancy of proof-of-concept testing of fast reactor fuels in cadmium-filtered positions in the ATR.

These observations and conclusions are summarized in Table 8.

Table 8. Summary of Conclusions Drawn from Analyses and Comparisons.

Phenomenon	Conclusion
Metallography/Ceramography	Good qualitative agreement observed for metallic and nitride fuels. Expected metallurgical phases and phase fields, which are highly temperature dependent, are present. For example, see direct comparison in Figure 69.
Neutron Radiography	Good qualitative agreement observed for metallic and nitride fuels relative to gross geometrical features and cracking patterns. Axial growth of metallic fuels appears exaggerated, likely due to very short fuel column heights used in ATR tests rather than differences caused by different neutron spectra.
Restructuring in Oxide Fuels	Excellent agreement expected based on detailed analyses. Future comparisons to PIE data from oxide fuels is needed to validate.
Constituent Redistribution in Metallic Fuels	TBD. Awaiting results from future EPMA analyses.

Axial Growth in Metallic Fuels	Differences observed between experiments, may be largely due to differences in fuel column heights between experiments. Phenomenon not known to be highly temperature depended.
Cladding Strain	Inconclusive. Experiments to date have not exhibited any significant cladding strain. However, stainless steel swelling and irradiation creep are expected to be neutron spectrum-dependent.
Gamma Ray Spectroscopy/Tomography	Good qualitative agreement observed. Strong indication of expected transport of Cs and Zr in metallic fuels.
Fission Gas Release	Very good quantitative agreement for a fuel performance parameter that can exhibit considerable scatter.
Burnup	Very good quantitative agreement.
Actinide Transmutation	Significant differences observed in quantities and relative abundances of non-fissile actinide isotopes, which are expected to be neutron spectrum-dependent.

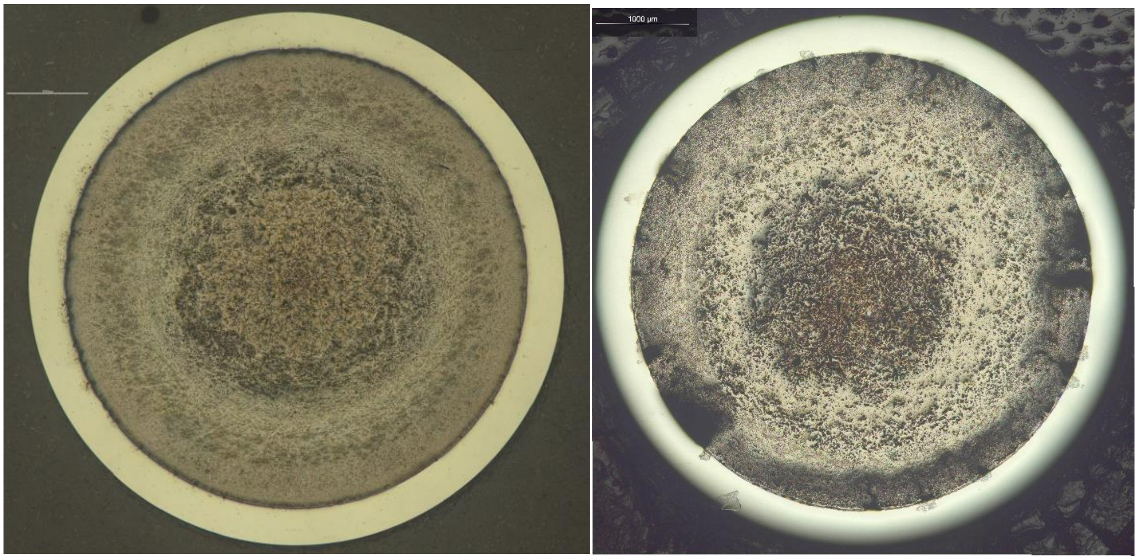

(a) (b)

Figure 69. Metallography of Pu-12Am-40Zr irradiated to approximately 20% burnup in: a) Phénix fast reactor (FUTURIX-FTA DOE2), and b) cadmium-filtered position in ATR (AFC-1D R4).

It is acknowledged that there are phenomena that cannot be reproduced properly in the cadmium-filtered test positions in ATR. Although the PIE data surveyed to date have not looked specifically at cladding performance, behaviors that are highly dependent on fast neutron flux/dose such as cladding swelling and creep will not be reproduced. In addition, data presented in this report on transmutation rates among the actinide (and especially minor actinide) isotopes, known to be highly dependent on neutron energies, shows that end of life isotopic mixtures can be very different between the two test environments. This means that no conclusions concerning minor actinide transmutation paths or rates can be drawn from the ATR tests and directly applied to fast reactor conditions; nevertheless, since fuel performance (i.e., material behavior) depends, in many cases, on the chemical distribution of elements, not isotopic distributions within elements, this result does not reflect negatively on objective of the cadmium-filtered testing in ATR, which focuses on the investigation of temperature-dependent material responses of fuels under irradiation.

Although the comparisons presented in this report are at this time limited in scope and preliminary in nature, and will be updated as future relevant data becomes available, they do support the assertion that the objectives of the cadmium-filtered testing approach in ATR are both feasible and appear sound. The analyses and comparisons presented in this report show that ATR irradiations performed using cadmium shrouding are sufficiently prototypic that they can be used with confidence in the development and testing of fast reactor fuels, although limited primarily to the investigation of those fuel performance phenomena that are primarily dependent on the conditions of temperature and/or temperature gradient within the fuel.

6. REFERENCES

1. Steven L. Hayes, Heather J. M. Chichester, Randall S. Fielding, Michael T. Benson, and W. Jon Carmack, “Transmutation Fuels Development in the Advanced Fuels Campaign,” Proceedings of Nuclear Fuels and Structural Materials for the Next Generation Nuclear Reactors (NFSM-2016), New Orleans, Louisiana, 12–16 June 2016.
2. Nuclear Energy Research and Development Roadmap, U.S. Department of Energy, https://www.energy.gov/sites/prod/files/NuclearEnergy_Roadmap_Final.pdf, 2010.
3. W.J. Carmack, L.A. Braase, R.A. Wigeland, M. Todosow, “Technology Readiness Levels for Advanced Nuclear Fuels and Materials Development,” Nuclear Engineering and Design, 313 (2017) 177–184.
4. D. Crawford, D. Porter, S. Hayes, M. Meyer, D. Petti, K. Pasamehmetoglu, “An Approach to Fuel Development and Qualification, Journal of Nuclear Materials, 371 (2007) 232–242.
5. S. Blaine Grover, “Testing of Gas Reactor Fuel and Materials in the Advanced Test Reactor,” Proceedings of the Pacific Basin Nuclear Conference, Sydney, Australia, 20-25 October 2006.
6. Gray S. Chang, “Cadmium Depletion Impacts on Hardening Neutron Spectrum for Advanced Fuel Testing in ATR,” Proceedings of the International Conference on Mathematics and Computational Methods Applied to Nuclear Science and Engineering (M&C 2011), Rio de Janeiro, Brazil, 8-12 May 2011.
7. G.S. Chang, R.G. Ambrosek, “Hardening Neutron Spectrum for Advanced Actinide Transmutation Experiments in the ATR,” Radiation Protection Dosimetry, 115 (2005) 63-68.
8. Ch. de Raedt, E. Malambu, B. Verboomen, Th. Aoust, “Increasing Complexity in the Modeling of BR2 Irradiations,” Proceedings of Advances in Reactor Physics and Mathematics and Computation into the Next Millennium (PHYSOR 2000), Pittsburgh, PA, 7-11 May 2000.
9. D. R. Olander, “Fundamental Aspects of Nuclear Reactor Fuel Elements,” Energy Research and Development Administration (ERDA) Technical Document TID-26711-P1, 1976.
10. Y. S. Tang, R. D. Coffield, R. A. Markley, Thermal Analysis of Liquid-Metal Fast Breeder Reactors, p. 225, 1978
11. “Phenix and Super-Phenix reactors,” IAEA-TECDOC—1569, International Atomic Energy Agency (IAEA), 2007, https://inis.iaea.org/search/search.aspx?orig_q=RN:39050386
12. “FY2009 Advanced Test Reactor National Scientific User Facility User’s Guide,” INL/EXT-08-14709, Idaho National Laboratory, 2009, https://nsuf.inl.gov/File/ATRUsersGuide.pdf
13. B. Hilton, D. Porter, S. Hayes, “AFC-1 Transmutation Fuels Post-Irradiation Hot Cell Examination 4 to 8 at.% Final Report; Irradiation Experiments AFC-1B, AFC-1F and AFC-1Æ,” INL/EXT-05-00785, Rev. 1, September 2006.
14. H.J.M Chichester, D.L. Porter, B.A. Hilton, “Postirradiation Examination of AFC-1D, 1G, 1H, and 2A Experiments,” INL/LTD-11-23242, Rev. 0, September 2011.
15. G.L. Hofman, L.C. Walters, T.H. Bauer, Metallic fast reactor fuels, Progress in Nuclear Energy, Volume 31, Issues 1–2, 1997, Pages 83-110, ISSN 0149-1970, http://dx.doi.org/10.1016/0149-1970(96)00005-4.
16. G.L. Hofman, S.L. Hayes, M.C. Petri, Temperature gradient driven constituent redistribution in U-Zr alloys, Journal of Nuclear Materials, Volume 227, Issue 3, January 1996, Pages 277-286, ISSN 0022-3115, http://dx.doi.org/10.1016/0022-3115(95)00129-8.

17. Douglas C. Crawford, Douglas L. Porter, Steven L. Hayes, Fuels for sodium-cooled fast reactors: US perspective, Journal of Nuclear Materials, Volume 371, Issues 1–3, 15 September 2007, Pages 202-231, ISSN 0022-3115, http://dx.doi.org/10.1016/j.jnucmat.2007.05.010.

18. W.J. Carmack, D.L. Porter, Y.I. Chang, S.L. Hayes, M.K. Meyer, D.E. Burkes, C.B. Lee, T. Mizuno, F. Delage, J. Somers, Metallic fuels for advanced reactors, Journal of Nuclear Materials, Volume 392, Issue 2, 15 July 2009, Pages 139-150, ISSN 0022-3115, http://dx.doi.org/10.1016/j.jnucmat.2009.03.007.

19. T. Ogata, 3.01 - Metal Fuel, In Comprehensive Nuclear Materials, edited by Rudy J.M. Konings,, Elsevier, Oxford, 2012, Pages 1-40, ISBN 9780080560335, http://dx.doi.org/10.1016/B978-0-08-056033-5.00049-5

20. Y. Arai, 3.02 - Nitride Fuel, In Comprehensive Nuclear Materials, edited by Rudy J.M. Konings,, Elsevier, Oxford, 2012, Pages 41-54, ISBN 9780080560335, http://dx.doi.org/10.1016/B978-0-08-056033-5.00050-1

21. J.M. Harp, H.J.M. Chichester, L. Capriotti, “Baseline Postirradiation Examination of the FUTURIX-FTA Experiments,” Idaho National Laboratory Report, INL/LTD-16-40088, (2016)

22. Jin Sik Cheon, Chan Bock Lee, Byoung Oon Lee, J.P. Raison, T. Mizuno, F. Delage, J. Carmack, Sodium fast reactor evaluation: Core materials, Journal of Nuclear Materials, Volume 392, Issue 2, 15 July 2009, Pages 324-330, ISSN 0022-3115, http://dx.doi.org/10.1016/j.jnucmat.2009.03.021

23. Gavoille, P., et al. “Mechanical properties of cladding and wrapper materials for the ASTRID Fast-Reactor Project.” Proc. of the IAEA International Conference on Fast Reactors and related Fuel Cycles: Safe Technologies and Sustainable Scenarios. 2013.

24. J. R. Kennedy, “FUTURIX-FTA Metal Alloy Fuel Fabrication and Characterization Report,” INL Report INL/EXT-07-12234 (2007).

25. S. Voit, K. McClellan, R. Margevicius, C. Stanek, and H. Hawkins, “The Design and Production of Actinide Nitride Fuels at the Los Alamos National Laboratory for the Advanced Fuel Cycle Initiative Program,” LANL Report LA-UR-06-4930 (2006).

26. I. Munoz, C. Repetto, B. Valentin, “Irradiation Report of the FUTURIX-FTA Metal Capsule,” Note Technique, CEA/DEN/CAD/DEC/SESC/LC2I NT 12-020 – Indice 1, Commissariat à l’Energie Atomique et aux Energies Alternatives (CEA) Report, CEA Cadarache, June 2014

27. I. Munoz, C. Repetto, B. Valentin, “Irradiation Report of the FUTURIC-FTA Nitride Capsule,” Note Technique, CEA/DEN/CAD/DEC/SESC/LC2I NT 09-004 – Indice 2, Commissariat à l’Energie Atomique et aux Energies Alternatives (CEA) Report, CEA Cadarache, June 2014

28. D.L. Porter, Hanchung Tsai, Full-length U–xPu–10Zr (x=0, 8, 19wt.%) fast reactor fuel test in FFTF, In Journal of Nuclear Materials, Volume 427, Issues 1–3, 2012, Pages 46-57, ISSN 0022-3115, https://doi.org/10.1016/j.jnucmat.2012.03.047

29. J.M. Harp, P.A. Demkowicz, “Investigation of the Feasibility of Utilizing Gamma Emission Computed Tomography in Evaluating Fission Product Migration in Irradiated TRISO Fuel Experiments,” Proceedings of HTR 2014, Weihai, China, October 27-31 2014

30. John D. Hunn, Charles A. Baldwin, Tyler J. Gerczak, Fred C. Montgomery, Robert N. Morris, Chinthaka M. Silva, Paul A. Demkowicz, Jason M. Harp, Scott A. Ploger, Detection and analysis of particles with failed SiC in AGR-1 fuel compacts, Nuclear Engineering and Design, Volume 306, September 2016, Pages 36-46, http://dx.doi.org/10.1016/j.nucengdes.2015.12.011

31. Jason M. Harp, Heather J.M. Chichester, “Highlights from the Postirradiation Examination of AFC-3A and AFC-3B.” *Transactions of the American Nuclear Society*, vol. 114, 2016

32. Personal Communication, Douglas C. Porter, X419 PIE archive data
33. R.S. Fielding, "FUTURIX-FTA Short Fuel Pin Welding Procedure," Idaho National Laboratory Record, W7520-0709-ES-00, Rev. 0, July 2006
34. R.G. Pahl, D.L. Porter, D.C. Crawford, L.C. Walters, Irradiation behavior of metallic fast reactor fuels, Journal of Nuclear Materials, Volume 188, 1992, Pages 3-9, http://dx.doi.org/10.1016/0022-3115(92)90447-S
35. Maeck, W.J., Larsen, R.P., Rein, J.E., "Burnup Determination for Fast Reactor Fuels: A Review and Status of the Nuclear Data and Analytical Chemistry Methodology Requirements," NTIS Report TID 26209, 1973
36. J.M. Harp, P.A. Demkowicz, P.L. Winston, J.W. Sterbentz, "An analysis of nuclear fuel burnup in the AGR-1 TRISO fuel experiment using gamma spectrometry, mass spectrometry, and computational simulation techniques," Nuclear Engineering and Design, 278, 395-405, (2014) http://dx.doi.org/10.1016/j.nucengdes.2014.07.041
37. Chadwick, M. B., et al. "ENDF/B-VII. 1 nuclear data for science and technology: cross sections, covariances, fission product yields and decay data." Nuclear Data Sheets 112.12: 2887-2996. 2011
38. D.E. Janney, C.A. Papesch, "2015. *FCRD Transmutation Fuels Handbook 2015,"* Idaho National Laboratory Report, INL/EXT-15-36520, Idaho National Laboratory (INL), Idaho Falls, ID (United States).
39. Yeon Soo Kim, G.L Hofman, S.L Hayes, Y.H Sohn, Constituent redistribution in U–Pu–Zr fuel during irradiation, Journal of Nuclear Materials, Volume 327, Issue 1, 2004, Pages 27-36, ISSN 0022-3115, http://dx.doi.org/10.1016/j.jnucmat.2004.01.012.
40. C.L. TRIBUS, J.E. SANESKI, S.P. HENSLEE, "Casting of metallic fuel containing minor actinide additions," *J. Nucl. Mater*., 204, 50 (2008).
41. M.K. MEYER, S. L. HAYES, W. J. CARMACK, H. TSAI, "The EBR-II X501 minor actinide burning experiment," *J. Nucl. Mater*., 392, 176 (2009).